The Astronomical Journal, 165:120 (20pp), 2023 March https://doi.org/10.3847/1538-3881/acabce

TOI-5205b: A Short-period Jovian Planet Transiting a Mid-M Dwarf

Shubham Kanodia[1,2,3], Suvrath Mahadevan[2,3,4], Jessica Libby-Roberts[2,3], Gudmundur Stefansson[25,5], Caleb I. Cañas[2,3,6,26], Anjali A. A. Piette[1], Alan Boss[1], Johanna Teske[1], John Chambers[1], Greg Zeimann[7], Andrew Monson[8], Paul Robertson[9], Joe P. Ninan[10], Andrea S. J. Lin[2,3], Chad F. Bender[8], William D. Cochran[11,12], Scott A. Diddams[13,14,15], Arvind F. Gupta[2,3], Samuel Halverson[16], Suzanne Hawley[17], Henry A. Kobulnicky[18], Andrew J. Metcalf[19], Brock A. Parker[18], Luke Powers[2,3], Lawrence W. Ramsey[2,3], Arpita Roy[20,21], Christian Schwab[22], Tera N. Swaby[18], Ryan C. Terrien[23], and John Wisniewski[24]

[1] Earth and Planets Laboratory, Carnegie Institution for Science, 5241 Broad Branch Road, NW, Washington, DC 20015, USA; shbhuk@gmail.com
[2] Department of Astronomy & Astrophysics, 525 Davey Laboratory, The Pennsylvania State University, University Park, PA 16802, USA
[3] Center for Exoplanets and Habitable Worlds, 525 Davey Laboratory, The Pennsylvania State University, University Park, PA 16802, USA
[4] ETH Zurich, Institute for Particle Physics & Astrophysics, Switzerland
[5] Department of Astrophysical Sciences, Princeton University, 4 Ivy Lane, Princeton, NJ 08540, USA
[6] NASA Goddard Space Flight Center, 8800 Greenbelt Road, Greenbelt, MD 20771, USA
[7] Hobby Eberly Telescope, University of Texas, Austin, Austin, TX 78712, USA
[8] Steward Observatory, The University of Arizona, 933 N. Cherry Avenue, Tucson, AZ 85721, USA
[9] Department of Physics & Astronomy, University of California Irvine, Irvine, CA 92697, USA
[10] Department of Astronomy and Astrophysics, Tata Institute of Fundamental Research, Homi Bhabha Road, Colaba, Mumbai 400005, India
[11] McDonald Observatory and Department of Astronomy, The University of Texas at Austin, USA
[12] Center for Planetary Systems Habitability, The University of Texas at Austin, USA
[13] Electrical, Computer & Energy Engineering, University of Colorado, 425 UCB, Boulder, CO 80309, USA
[14] Department of Physics, University of Colorado, 2000 Colorado Avenue, Boulder, CO 80309, USA
[15] Time and Frequency Division, National Institute of Standards and Technology, 325 Broadway, Boulder, CO 80305, USA
[16] Jet Propulsion Laboratory, 4800 Oak Grove Drive, Pasadena, CA 91109, USA
[17] Department of Astronomy, Box 351580, University of Washington, Seattle, WA 98195, USA
[18] Department of Physics & Astronomy, University of Wyoming, Laramie, WY 82070, USA
[19] Space Vehicles Directorate, Air Force Research Laboratory, 3550 Aberdeen Avenue SE, Kirtland AFB, NM 87117, USA
[20] Space Telescope Science Institute, 3700 San Martin Drive, Baltimore, MD 21218, USA
[21] Department of Physics and Astronomy, Johns Hopkins University, 3400 N Charles Street, Baltimore, MD 21218, USA
[22] School of Mathematical and Physical Sciences, Macquarie University, Balaclava Road, North Ryde, NSW 2109, Australia
[23] Carleton College, One North College Street, Northfield, MN 55057, USA
[24] Department of Physics & Astronomy, George Mason University, 4400 University Drive, MS 3F3, Fairfax, VA 22030, USA
Received 2022 September 22; revised 2022 November 30; accepted 2022 December 15; published 2023 February 21

Abstract

We present the discovery of TOI-5205b, a transiting Jovian planet orbiting a solar metallicity M4V star, which was discovered using Transiting Exoplanet Survey Satellite photometry and then confirmed using a combination of precise radial velocities, ground-based photometry, spectra, and speckle imaging. TOI-5205b has one of the highest mass ratios for M-dwarf planets, with a mass ratio of almost 0.3%, as it orbits a host star that is just 0.392 ± 0.015 $M_{\odot}$. Its planetary radius is 1.03 ± 0.03 $R_{\rm J}$, while the mass is 1.08 ± 0.06 $M_{\rm J}$. Additionally, the large size of the planet orbiting a small star results in a transit depth of ∼7%, making it one of the deepest transits of a confirmed exoplanet orbiting a main-sequence star. The large transit depth makes TOI-5205b a compelling target to probe its atmospheric properties, as a means of tracing the potential formation pathways. While there have been radial-velocity-only discoveries of giant planets around mid-M dwarfs, this is the first transiting Jupiter with a mass measurement discovered around such a low-mass host star. The high mass of TOI-5205b stretches conventional theories of planet formation and disk scaling relations that cannot easily recreate the conditions required to form such planets.

Unified Astronomy Thesaurus concepts: Radial velocity (1332); M dwarf stars (982); Extrasolar gaseous giant planets (509); Transits (1711)

Supporting material: data behind figure

1. Introduction

M dwarfs are the most common type of stars in the Galaxy (Henry et al. 2006; Reylé et al. 2021), and host a higher number of planets on average compared to FGK stars (Mulders et al. 2015). Yet due to their lower stellar (and disk) masses—and associated slower formation timescales—gas giants are expected to be infrequent around M dwarfs (Laughlin et al. 2004; Ida & Lin 2005). Recently, Burn et al. (2021) generated a synthetic planet population across a range of stellar masses and metallicities, to find that nominal scaling relations for disk properties and migration rates cannot reproduce the existence of gas giants for stellar masses <0.5 $M_{\odot}$.

New discoveries from the Transiting Exoplanet Survey Satellite (TESS; Ricker et al. 2014) have helped find numerous gas giants around M dwarfs despite their rarity (e.g., Cañas et al. 2020, 2022; Jordán et al. 2022; Kanodia et al. 2022), by

[25] Henry Norris Russell Fellow.
[26] NASA Postdoctoral Program Fellow.

observing millions of M dwarfs that are also bright enough for radial velocity (RV) mass measurements of transiting planet candidates (Stassun et al. 2018). Despite the enhanced detection signatures, the sample of confirmed transiting gas giants with precise mass measurements around M dwarfs consists of only <10 planets. All of these transiting gas giants around M dwarfs orbit early-M host stars, most of which are also metal-rich stars (Gan et al. 2022; Kanodia et al. 2022). These trends agree with the mass budget argument, which necessitates massive stars (and disks) with high dust content to form the 10 $M_{\oplus}$ cores (Pollack et al. 1996) in a timely manner before the disk dissipates. The alternative formation mechanism invokes disk instabilities for massive protoplanetary disks to form these gas giants more quickly (Boss 2006).

However, as we move from early-M dwarfs toward the mid-M dwarfs, the internal structures of these stars change (Limber 1960). Around 0.35 $M_{\odot}$, the partially convective M dwarfs (convective core + radiative envelope + convective outer envelope) transition to fully convective stars. This transition is associated with slow oscillations in stellar properties (radius, luminosity, etc.), which can potentially impact the orbital evolution of planets around these stars (VanderPlas 2018; Feiden et al. 2021). In this manuscript, we present the discovery of the first transiting Jovian exoplanet, which also has a mass measurement, orbiting a mid-M dwarf—TOI-5205.

To characterize the host star and confirm the planetary nature of TOI-5205b, we use a combination of TESS and ground-based photometry (RBO, TMMT, and APO/ARCTIC), high-contrast speckle imaging (WIYN/NESSI), precision RVs from the Habitable-zone Planet Finder spectrograph (HPF) and low-resolution optical spectra from the Low Resolution Spectrograph 2 (LRS2). In Section 2 we detail these observations, while in Section 3 we discuss the stellar parameters. Subsequently, in Section 4 we detail the data analysis, including the joint fitting of the photometry and RVs. In Section 5 we discuss the mass budget for protoplanetary disks that would be required to form such a massive planet, and place it in context of other planets around M dwarfs. Finally, we summarize our findings in Section 6.

2. Observations

2.1. TESS

TOI-5205 (TIC-419411415, Gaia DR3 1842656663520849024) is a mid-M dwarf observed by TESS in Sector 15 in Camera 1 (Figure 1) from 2019 August 15 to 2019 September 11 at ∼30 minutes cadence (Figure 2(a)), and Sector 41 in Camera 1 from 2021 July 23 to 2021 August 20 at ∼10 minutes cadence (Figure 2(b)). The planet candidate was identified using the Quick Look Pipeline algorithm developed by Huang et al. (2020), under the "faint-star search" (Kunimoto et al. 2022) with a period of ∼1.63 days.

We extract the light curve from the TESS full-frame images (FFIs) using using `eleanor` (Feinstein et al. 2019), which uses the TESScut[27] service to obtain a cut-out of 31 × 31 pixels from the calibrated FFIs centered on TOI-5205. The light curve is derived from the `CORR_FLUX` values, in which `eleanor` uses linear regression with pixel position, measured background, and time to remove signals correlated with these

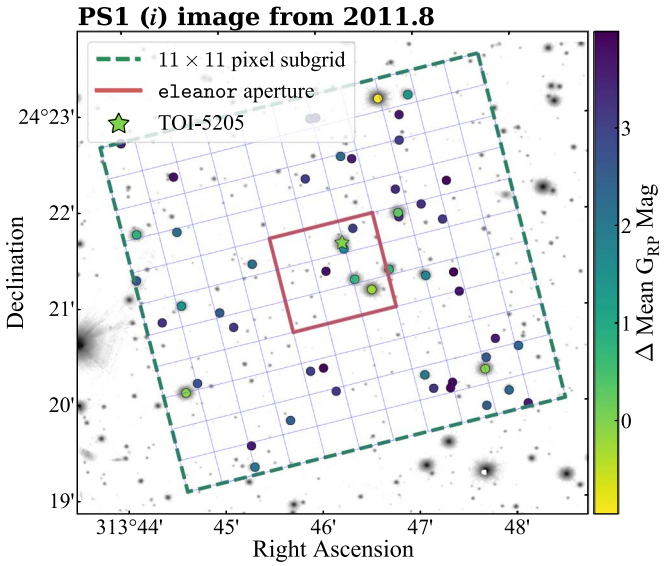

Figure 1. We overlay an 11 × 11 pixel footprint from TESS Sector 15 (blue grid) on a Pan-STARRS1 image from ∼2011 (Evans et al. 2016b). The TESS aperture is outlined in red, and we highlight TOI-5205 with a star. Each TESS pixel is ∼21″ in size. The TESS observations of TOI-5205 are contaminated by the presence of background stars, thereby necessitating ground-based transits to constrain the true transit depth.

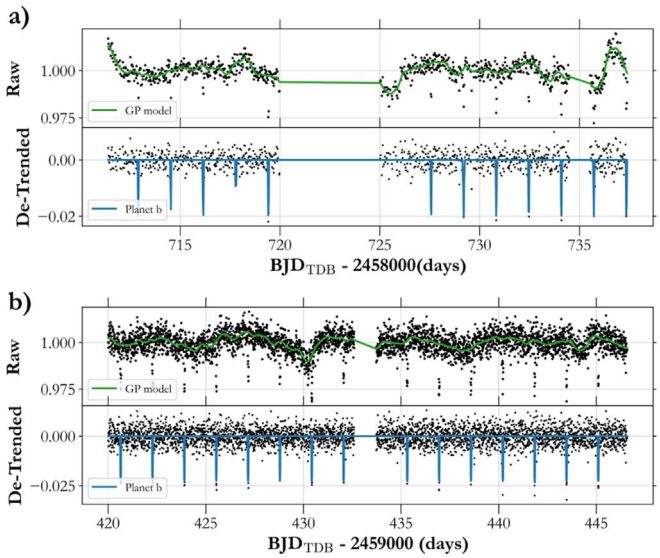

Figure 2. Time series plot for TESS based on long cadence `eleanor` photometry from Sector 15 (panel (a) with 1800 s exposure time) and Sector 41 (panel (b) with 600 s exposure time), along with a stellar rotation Gaussian process (GP) kernel (`RotationTerm` from `celerite2`) in green. The detrended (GP subtracted) photometry is shown in the bottom panel, with the TOI-5205b transits overlaid in blue.

parameters. The default aperture is a 2 × 1 pixel rectangle, which does not include the target star. Instead, we set the `aperturemode` to "large" in `eleanor`, which uses a 3 × 3 pixel square aperture that includes the target star and obtains a combined differential photometric precision (CDPP) of ∼3850 and ∼4730 ppm for the two sectors, respectively (Figure 2). The CDPP is formally the rms of the photometric noise on transit timescales, and was originally defined for Kepler (Jenkins et al. 2010). We also try a custom aperture in `eleanor` of size 2 × 1 pixels, which includes only the two top-right pixels from the large aperture shown below. This

[27] https://mast.stsci.edu/tesscut/

Table 1
Summary of Ground-based Photometric Follow-up

Obs Date (YYYY-MM-DD)	Filter	Exposure Time (s)	PSF FWHM (″)	Field of View (′)
		RBO (0.6 m)		
2022-05-10	Bessell I	240	2.6–6.0	8.94×8.94
		TMMT (0.3 m)		
2022-05-15	Bessell I	180	3.8–4.5	40.75×40.75
		APO (3.5 m)		
2022-04-22	SDSS i'	5	2.0–3.2	7.9×7.9
2022-07-03	SDSS g'	40	1.4–2.2	7.9×7.9
2022-07-16	SDSS i'	20	3.4–8.3	7.9×7.9

gives us comparable posteriors to the photometry fit, while having a slightly degraded CDPP. For subsequent analysis, we use the "large" aperture shown in Figure 1.

TOI-5205 is present in a crowded field with 10 stars located $<30''$ away, with the closest star (TIC 1951446034) located about 4.″2 away and ∼1.7 mag fainter in the TESS bandpass (Figure 1). Based on Gaia DR3 astrometry, TIC 1951446034 is not comoving and is instead ∼30× more distant than TOI-5205 (∼2300 pc; Vallenari et al. 2022). The `eleanor` aperture includes many of these field stars, which present a significant source of dilution to the TESS light curve and necessitate ground-based follow-up that can resolve these background stars. We discuss this dilution further in Section 4 where we include a dilution term while fitting the TESS photometry.

2.2. Ground-based Transit Follow-up

2.2.1. 3.5 m ARC Telescope

We observed three transits of TOI-5205b using the Astrophysical Research Consortium (ARC) Telescope Imaging Camera (ARCTIC; Huehnerhoff et al. 2016) at the ARC 3.5 m Telescope at Apache Point Observatory (APO) on the nights of 2022 April 22, 2022 July 3, and 2022 July 16. All of these observations were conducted using quad-amplifier and fast readout mode using 4×4 on-chip binning mode to achieve a gain of 2 e^- ADU^{-1}, a plate scale of 0.″456 $pixel^{-1}$, and a readout time of 2.7 s. The relevant observation parameters are included in Table 1.

2022 April 22: We observed an ingress of TOI-5205b (Figure 3(c)) in the Sloan Digital Sky Survey (SDSS) i' while the target was rising from an airmass of 1.41–1.16. To spatially resolve and separate out the background star (∼4.″2 away), we moderately defocus the star instead of using the engineered diffuser available on ARCTIC (Stefansson et al. 2017). These observations were conducted toward the end of the night, with the transit being interrupted by morning twilight. To prevent saturating the detector with the bright sky, we used a short exposure time of 5 s. We processed the photometry using `AstroImageJ` (Collins et al. 2017) and the final reduction used a photometric aperture radius of 6 pixels (2.″74), an inner sky radius of 15 pixels (6.″8), and an outer sky radius of 25 pixels (11.″4). This small innermost annulus separates TOI-5205 and the closest background star (∼4.″2). Furthermore, to verify the transit depth we also perform point-spread function (PSF) photometry (instead of aperture photometry; following the routine described in Section 2.3), and obtain a comparable transit depth as that from the procedure followed above using aperture photometry.

2022 July 3: To check for chromaticity (Appendix A.4.2), we also observed TOI-5205b on 2022 July 3 (Figure 3(d)) in SDSS g' while it was rising from an airmass of 2.35–1.45. Similar to the previous observation, we do not use a diffuser, and moderately defocus the star. The data was reduced using aperture photometry in `AstroImageJ` using the same annuli as above. We detrend this photometry with the FWHM of the target star across the night. The observation was interrupted due to increasing humidity and cloudy conditions, which forced us to stop observing shortly after transit midpoint.

2022 July 16: We obtained a full transit of TOI-5205b on 2022 July 16 (Figure 3(g)) while it was rising from an airmass of 2.69–1.01 in SDSS i'. During these observations the telescope secondary mirror had hardware issues that prevented us from using the focuser. This led to the stellar PSF changing by ∼2× during the night, which caused significant systematics in the photometry that had to be detrended out by the airmass and FWHM during the night. Due to the lack of focuser control, our PSF FWHM is much larger than on previous nights, necessitating larger aperture radii of 12, 18, and 25 pixels or 5.″5, 8.″2, and 11.″4, respectively. The large science aperture includes varying levels of contamination from the closest background star across the night. We therefore do not use this data set to refine our transit depth, but only the ephemeris.

2.2.2. 0.6 m RBO

We observed a transit of TOI-5205b on 2022 May 10 (Figure 3(e)) using the 0.6 m telescope at the Red Buttes Observatory (RBO) in Wyoming (Kasper et al. 2016). The RBO telescope is an $f/8.43$ Ritchey–Chrétien Cassegrain constructed by DFM Engineering, Inc.

The target rose from an airmass of 2.1–1.1. The observations were performed using the Bessell I filter with 2×2 pixel on-chip binning and exposure times of 240 s. The binned plate scale for RBO is 0.″73 $pixel^{-1}$.

2.2.3. 0.3 m TMMT

We observed a transit on 2022 May 15 (Figure 3(f)) using the using the Three-hundred MilliMeter (300 mm) Telescope (TMMT; Monson et al. 2017) at Las Campanas Observatory in Chile. TMMT is an $f/7.8$ FRC300 from Takahashi on a German equatorial AP1600 GTO mount with an Apogee Alta U42-D09 CCD Camera, FLI ATLAS focuser, and Centerline filter wheel.

The target rose from an airmass of 4.88 at the start of observations to a minimum airmass of 1.67, and then set to an airmass of 1.69 at the end of the observations. The observations were performed using Bessell I filter with 1×1 on-chip binning and exposure times of 180 s. In the 1×1 binning mode, TMMT has a gain of 1.35 e ADU^{-1}, a plate scale of 1.″194 $pixel^{-1}$, and a readout time of 6 s.

Considering the dilution from the neighboring companion, we use the RBO, TMMT, and third ARCTIC transits only to refine the ephemeris, and not to estimate the transit depth (shown in red in Figure 3).

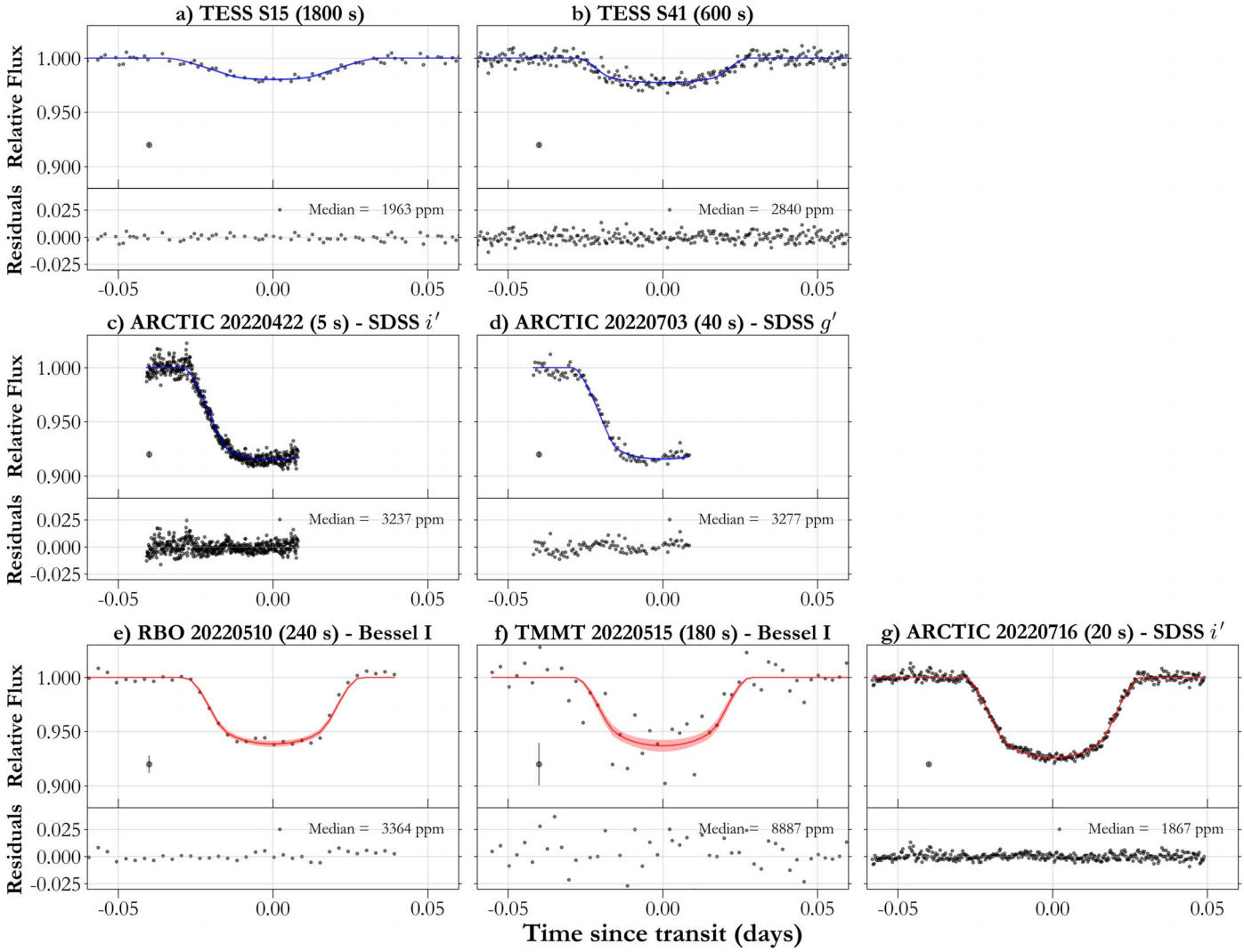

Figure 3. Photometric observations for TOI-5205b; in all of the plots, the gray points show the detrended data, while the model is shown in color, along with the 1σ confidence intervals as translucent bands. We also include the representative median statistical uncertainty at $x = -0.04$, but the error bar is smaller than the point for certain instruments. (a)–(b) The TESS light curve phase-folded to the best-fit orbital period for sectors 15 and 41, respectively. (c)–(d) Ground-based observations from ARCTIC for TOI-5205b that are used to estimate transit depth, shape, and ephemeris (The data behind the ARCTIC transits is included along with the manuscript). (e)–(g) The RBO transit from 2022 May 10, TMMT transit from 2022 May 15, and the ARCTIC transit for 2022 July 16 are included to improve the ephemeris estimate, but not to estimate the transit depth (model shown in red) because of dilution from the background companion (Section 2.2).

(The data used to create this figure are available.)

2.3. *Estimating* JHK *Magnitudes Using FourStar*

We acquired near-infrared (NIR) imaging using the FourStar Infrared Camera on the 6.5 m Magellan Baade telescope (Persson et al. 2013) during the night of 2022 July 13. The plate scale for FourStar is $0\farcs16$ per pixel, while the seeing during observations was $\sim 0\farcs9$, which was useful to clearly separate the nearby background sources in a short 2.911 s exposure in the *J*, *H*, and *Ks* filters. Each filtered observation used a five-point dice-5 dither pattern and processed using a custom FourStar reduction package. We used the `daophot` suite of programs to perform PSF fitting photometry (Stetson 1987; Stetson & Harris 1988). The PSF photometry was compared to un-blended Two Micron All Sky Survey (2MASS) stars in the field to determine the photometric zero-points in each filter. The final *JHK* magnitudes are listed in Table 3.

2.4. *Speckle Imaging with NESSI at WIYN*

To search for faint stellar companions or background sources that might have contributed to or diluted the detected transit signal, we acquired observations of TOI-5205 with the NN-EXPLORE Exoplanet Stellar Speckle Imager (NESSI; Scott et al. 2018) on the WIYN 3.5 m telescope at Kitt Peak National Observatory on 2021 May 5. A sequence of 40 ms diffraction-limited images was taken in the Sloan z' filter during the 9 minute observation, and these were then reconstructed following the procedures described by Howell et al. (2011). We detect no nearby sources with magnitudes brighter than $\Delta z' = 4.0$ for separations $>0\farcs3$. The contrast curve and reconstructed speckle image are shown in Figure 4.

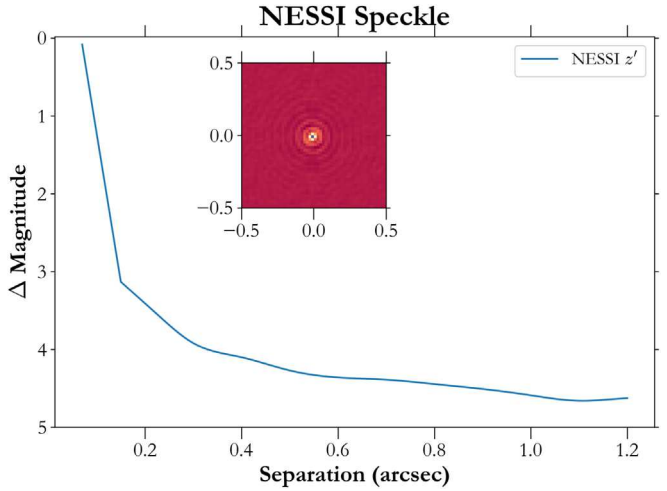

Figure 4. 5σ contrast curve for TOI-5205 observed from NESSI in the Sloan z' filter showing no bright companions within 1.″2 from the host star. The z' image is shown as an inset 1″ across.

2.5. LRS2

To confirm the spectral type and stellar parameters for TOI-5205, we also observe the target using LRS2 (Lee et al. 2010; Evans et al. 2016a) on the Hobby-Eberly Telescope (HET; Ramsey et al. 1998) at McDonald Observatory, in West Texas. LRS2 is a low-resolution ($R \sim 1900$) optical integral field unit spectrograph composed of two arms that simultaneously observe two $6'' \times 12''$ fields of view separated by 100″. The blue arm (LRS2-B) consists of a pair of channels with spectral ranges of ∼3640–4670 and ∼4540–7000 Å, while the red arm (LRS2-R) is composed of two channels covering ∼6430–8450 and ∼8230–10560 Å. The LRS2-R data were obtained with an 1800 s exposure on 2022 June 11 (1.″4 seeing), while the LRS2-B data were taken on 2022 August 3 (1.″6 seeing) with the same exposure time.

The raw data were processed with `Panacea`,[28] an automated reduction pipeline for LRS2 written by G. Zeimann et al. (2022, in preparation). The initial processing includes bias-correction, wavelength calibration from arc lamps taken within seven nights of the observation, fiber trace calculation from flat field exposures over ±7 nights, fiber normalization from twilight exposures over ±7 nights, fiber extraction, and an initial flux calibration from default response curves and measures of the mirror illumination as well as the exposure throughput from guider images. After the initial reduction, we used `LRS2Multi`,[29] a `python` interface to perform advanced reduction steps and calibrations for `Panacea` products. Using `LRS2Multi`, we identified the target star, defined a 3.″5 aperture, and used fibers beyond that aperture to build our sky model for each exposure. We subtracted the initial sky, and then constructed a principle component basis of 25 components with the residuals to further subtract sky residuals that occur from variable spectral PSFs for each fiber. This is especially important for the LRS2-R channels. We extracted the target spectrum from the sky-subtracted frames and normalized the LRS2-B to the LRS2-R spectrum using a 100 Å window in the overlap between the two spectrographs. Noting that the default response may not be accurate enough for spectrophotometry, we reduced and calibrated standard stars from 2021 June through 2022 August and measured the average flux calibration correction. The response correction was smoothed by a median filter with a 250 pixel kernel and was applied to our extracted spectrum. The correction was relatively small and smoothly declining with a ∼10% positive correction in blue and a ∼10% negative correction in red. Finally, the telluric correction was chosen from three empirical models constructed from a dozen HR telluric standard stars. We note that the relative chromatic flux calibration should be good to ∼5% for ∼3700–10200 Å based on the standard star analysis above, with the exception of regions with strong telluric absorption and where individual channels overlap. The final LRS2 spectra was used to estimate the spectral type of the star (Appendix A.1).

2.6. Radial Velocity Follow-up with HPF

We started RV observations of TOI-5205 with HPF (Mahadevan et al. 2012; Ramsay et al. 2014) on 2022 April 20. HPF is a high-resolution NIR (8080−12780 Å), fiber-fed (Kanodia et al. 2018) precision RV spectrograph with a stabilized environment (Stefansson et al. 2016). HPF is located at HET, which is a fixed-altitude telescope with a roving pupil design, and is fully queue-scheduled, where all of the observations are executed by the HET resident astronomers (Shetrone et al. 2007). We correct for bias, nonlinearity, cosmic rays, and calculate the slope/flux and variance images from the raw HPF data, using the algorithms described in the package `HxRGproc` (Ninan et al. 2018). We do not utilize simultaneous calibration using the NIR Laser Frequency Comb for HPF (Metcalf et al. 2019) due to concerns about the impact of scattered calibration light given the faintness of our target. Instead, we obtain a wavelength solution for the target exposures by interpolating the wavelength solution from other LFC exposures on the night of the observations. This has been shown to enable precise wavelength calibration and drift correction with a precision of ∼30 cm s^{-1} per observation (Stefansson et al. 2020), a value much smaller than our expected per-observation RV uncertainty (instrumental + photon noise) for this object of 22 m s^{-1} (in 969 s exposures, and 15 m s^{-1} in binned 30 minute exposures).

To derive the RVs from the extracted spectra, we use the template-matching method (e.g., Anglada-Escudé & Butler 2012). This has been implemented under the `SpEctrum Radial Velocity AnaLyser` pipeline (`SERVAL`; Zechmeister et al. 2018), which has since been modified for HPF (Stefansson et al. 2020). Under this method, we first create a master template from the target star observations, and then determine the Doppler shift for each individual observation by moving it in velocity space, comparing it with the template, and minimizing the χ^2 statistic. The master template is created using all of the HPF observations for TOI-5205, after masking out the telluric and sky-emission lines. The telluric regions are identified by a synthetic telluric-line mask generated from `telfit` (Gullikson et al. 2014), a Python wrapper to the Line-by-Line Radiative Transfer Model package (Clough et al. 2005). We use `barycorrpy` (Kanodia & Wright 2018) to perform the barycentric correction on the individual spectra, which is the Python implementation of the algorithms from Wright & Eastman (2014).

We obtained a total of seven visits on this target between 2022 April 20 and 2022 May 19 (Figure 5). Each visit was

[28] https://github.com/grzeimann/Panacea
[29] https://github.com/grzeimann/LRS2Multi

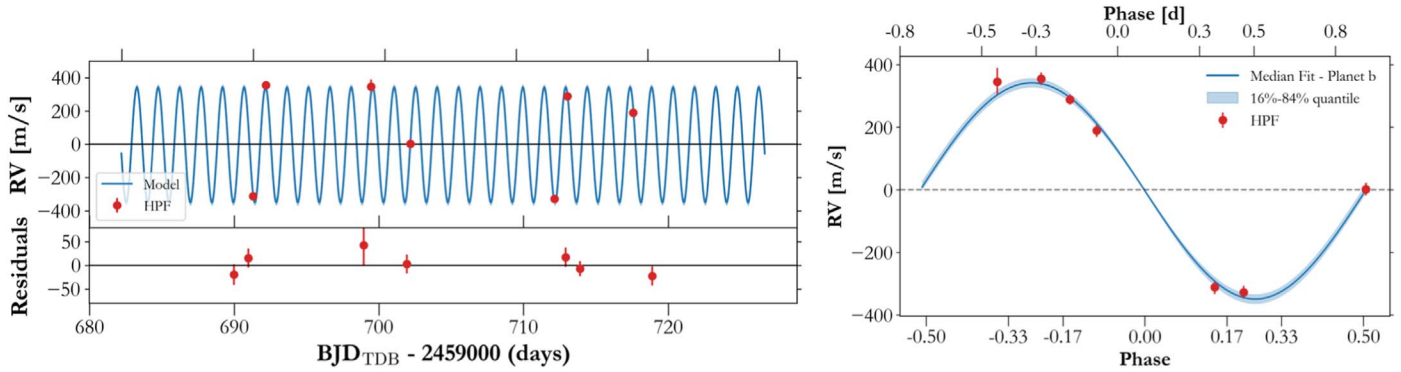

Figure 5. Left: time series of RV observations of TOI-5205 with HPF (red). The best-fitting model derived from the joint fit to the photometry and RVs is plotted in blue, including the 16%–84% confidence interval in lighter blue. The bottom panel shows the residuals after subtracting the model. Right: HPF RV observations phase-folded on the best-fit orbital period from the joint fit from Section 4. While we let the eccentricity float in this fit, the results are consistent with a circular orbit (Table 4).

divided into two exposures of 969 s each, where the median signal-to-noise ratio (S/N) of each HPF exposure was 40 per pixel at 1070 nm. The individual exposures were then combined by weighted averaging, with the final binned RVs being listed in Table 2.

Table 2
RVs (Binned in ∼30 minutes Exposures) of TOI-5205

BJD$_{TDB}$ (days)	RV (m s^{-1})	σ (m s^{-1})
2459689.97105	−339.74	21.68
2459690.96744	326.19	20.27
2459698.96070	317.19	43.67
2459701.93977	−26.88	20.05
2459712.90820	−355.59	20.44
2459713.90256	259.72	16.08
2459718.89386	160.39	19.95

3. Stellar Parameters

The stellar properties for TOI-5205 are crucial for understanding the system. Because it sits near this transition zone between fully and partially convective M dwarfs, the typical M dwarf scaling relations have additional scatter and often diverge. We have undertaken a thorough, multifaceted approach to constraining the stellar properties and testing their robustness, the details of which are included in Appendix A.2. We summarize the main results here. From Gaia magnitudes and LRS2 spectra, we estimate a spectral subtype of M4 ± 1 for TOI-5205. From photometric relations, we obtain an effective temperature of 3430 ± 54 K, solar metallicity, and a stellar radius of 0.394 ± 0.011 $R_{\odot}$. We then use a mass–radius relationship for M dwarfs to obtain a mass of 0.392 ± 0.015 $M_{\odot}$. We use Hα equivalent width measurements from LRS2 spectra and the lack of a detectable rotation period in the photometry to conclude that TOI-5205 is not an active star. Additionally, we rule out a number of false-positive scenarios (such as background and hierarchical eclipsing systems) using a combination of archival images, HPF spectra, NESSI high-contrast imaging, chromatic estimates of the transit depth. The procedure followed to perform this analysis and characterize the host star is explained in the Appendix.

3.1. Transition between Partially and Fully Convective Stars

M dwarfs with masses ∼0.35 $M_{\odot}$ have internal structures that transition from being partially convective (for the more massive stars) to fully convective (for the less-massive ones; Limber 1958; Baraffe & Chabrier 2018). On the more massive end, the partially convective stars have convective cores and envelopes separated by a radiative zone. As these stars fuse ^{3}He in the convective core, the ^{3}He abundance rises with temperature when in nonequilibrium (Figure 2; Baraffe & Chabrier 2018), and causes the convective core to increase in radius, and ultimately merge with the outer convective envelope that has a lower ^{3}He abundance (MacDonald & Gizis 2018; Feiden et al. 2021). This merger is accompanied by a sudden drop in the ^{3}He abundance in the core, which reduces the reaction rate, causing the core to contract and separate from the envelope (Figure 5 from Feiden et al. 2021). When the core contracts, the temperature begins to rise again, producing an increase in the abundance of ^{3}He, and an episodic cycling over gigayear timescales. Due to these repeated mergers and contractions, the abundance of the convective envelope increases until the core-envelope merger is not accompanied by a sudden decrease in abundance (and associated nuclear reaction rate). At this point, the star attains a fully convective steady state. The timescale to attain this fully convective state for stars in this transition zone depends on the mass and metallicity of the star (Kroupa & Tout 1997; Feiden et al. 2021). Unsurprisingly, these oscillations are accompanied by slow and small variations in the radius and luminosity of the star (van Saders & Pinsonneault 2012; MacDonald & Gizis 2018). This transition zone is also accompanied by an inflection in the mass–luminosity relation[30] for M dwarfs as was noted by Kroupa et al. (1990) and Delfosse et al. (2000). As an aside, this feature in the mass–luminosity relation causes a local maxima in the slope, which can reproduce the additional scatter in the $T_{\rm eff}$–R_* relation for mid-M dwarfs in Mann et al. (2015).

Based on Gaia DR2, Jao et al. (2018) presented the discovery of the now eponymous gap near $M_G \sim 10.2$ in the Gaia color–magnitude diagram (CMD; M_G versus $G_{\rm BP} - G_{\rm RP}$). This is a narrow diagonal region with an underdensity of stars, the width of which is a function of $G_{\rm BP} - G_{\rm RP}$ color (Jao & Feiden 2020). While the gap is associated with a 10%–20%

[30] Empirically this was first noticed as an increase in the stellar luminosity function for the local neighborhood $M_V \sim 11.5$, which was then attributed to the combination of a smooth initial mass function, and an inflection in the mass–luminosity relationship due to this transition.

decrement in the number of stars, it is hardly seen redward of $G_{BP} - G_{RP} \sim 2.7$. Theoretical models have been used to approximately reproduce the properties of the gap in the CMD relying on the ^{3}He instability, and attribute this underdensity to the transition between partial and fully convective M dwarfs (Feiden et al. 2021).

While TOI-5205 does not lie in this gap based on Gaia photometry, it is one of the few known planet-hosting stars in its vicinity, i.e., near this transition zone between fully and partially convective M dwarfs (Silverstein et al. 2022). TOI-5205 has a $G_{BP} - G_{RP}$ of $\sim$2.8, and M_G of $10.09^{+0.01}_{-0.03}$ from Gaia DR3, which would place it redward of this diagonal gap (M_G versus $G_{BP} - G_{RP}$ space). The background companion to TOI-5205 at $\sim 4''$ could contaminate the prism spectra used to obtain the color estimates. Creevey et al. (2022) mentioned that a CCD window of $3\farcs5 \times 2\farcs1$ is used while extracting the spectra, the orientation for which is quasi-random on the sky over different epochs. However the background companion is much hotter ($T_{\rm eff} \sim 5450$ K; Stassun et al. 2019) than TOI-5205 ($T_{\rm eff} \sim 3400$ K; Table 3), and therefore bluer.

4. Joint Fitting of Photometry and RVs

We perform a joint fit of the photometry and RVs using the `python` package `exoplanet` (Foreman-Mackey et al. 2021b), which relies on `PyMC3`, the Hamiltonian Monte Carlo (HMC) package (Salvatier et al. 2016). The HMC method has shown to be computationally efficient in spanning multi-dimensional parameter spaces to estimate parameter posteriors. The `exoplanet` package uses `starry` (Luger et al. 2019; Agol et al. 2020) to model the transits, and relies on the analytical models from Mandel & Agol (2002), and separate quadratic limb-darkening terms for each instrument. The limb-darkening priors use the reparameterization suggested by Kipping (2013) for uninformative sampling. We perform a joint fit with all of the photometry and RVs, where we fit each phased transit (Figure 3) with separate limb-darkening coefficients. We also include a simple-white noise model in the form a jitter term for each photometry data set. Our likelihood function for the TESS photometry includes a Gaussian Process (GP) kernel to model the quasiperiodic signal (Figure 2). This signal is discussed further in Appendix A.3.2.

We include a dilution term (Dil) in the photometric model to account for the presence of blended (or spatially unresolved) background stars in the TESS photometry. We assume that the higher spatial resolution ground-based photometry from the first two ARCTIC transits has no contamination from the background stars (i.e., Dil = 1), and therefore can be used to correct the TESS photometry. This dilution term is fit separately for individual TESS sectors, due to the different placement of the target and background stars on the camera pixels. We fit the dilution using a uniform prior from 0.1–1.5 to correct for potential overcompensation of the dilution term. While this is not a problem for the `eleanor` reduction, occasionally the SPOC data can overcorrect for dilution as shown for TOI-824 (Burt et al. 2020), especially in crowded fields. The dilution term (Dil) is used to inflate the planetary radius (R_p) estimate as shown below:

$$R_{p,\rm true} = \frac{R_{p,\rm TESS}}{\sqrt{\rm Dil}}. \quad (1)$$

The first two ARCTIC transits (ingress in i', g') are used to estimate the true transit depth. The ARCTIC data set from 2022 July 16 suffers from instrument systematics due to wildly varying PSF FWHM from a malfunctioning focuser. This manifests as varying levels of contamination from the nearby star. We use this ARCTIC data set along with the RBO and TMMT photometry to improve our ephemeris estimate.

Separate from the joint fit, we also use the ARCTIC data set from 2022 July 16 to estimate the eccentricity using the photoeccentric effect (Dawson & Johnson 2012), which relies on the transit duration and estimates and eccentricity of $0.11^{+0.32}_{-0.08}$. This is consistent with the eccentricity obtained from the RV orbit (albeit a weaker limit), and suggests a circular orbit, which is unsurprising for a giant planet at such a short orbital period, which would have a circularization timescale of $\sim$1 Myr. The precise photometry and duration estimate is then used to calculate a host star density assuming a circular orbit, to confirm the stellar parameters in Appendix A.2.

We model the RVs using a standard Keplerian model, allowing the eccentricity to float. We also include an RV offset and jitter term of HPF, along with a linear RV trend to account for long-term drifts (both instrumental and astrophysical). We use `scipy.optimize` to find the initial *maximum* a posteriori parameter estimates, which uses the default BFGS algorithm (Broyden–Fletcher–Goldfarb–Shanno algorithm; Broyden 1970; Fletcher 1970; Goldfarb 1970; Shanno 1970). These parameter estimates are then used as the initial conditions for parameter estimation using "No U-Turn Sampling" (Hoffman & Gelman 2014), implemented for the HMC sampler `PyMC3`, where we check for convergence using the Gelman–Rubin statistic ($\hat{R} \leqslant 1.1$; Ford 2006).

The final derived planet parameters from the joint fit are included in Table 4, with the phased RVs shown in Figure 5.

5. Discussion

While gas giants are predicted to be rare and hard to form under the core-accretion framework (Laughlin et al. 2004; Ida & Lin 2005), they do exist around M dwarfs, as has been evinced by recent discoveries from transiting surveys, especially TESS (Johnson et al. 2012; Hartman et al. 2015; Bayliss et al. 2018; Cañas et al. 2020, 2022; Jordán et al. 2022; Kanodia et al. 2022). In addition to transit discoveries, there have been RV-only detections of gas giants around M dwarfs, e.g., Johnson et al. (2010), Wittenmyer et al. (2014), Astudillo-Defru et al. (2017), Trifonov et al. (2018), Feng et al. (2020), Morales et al. (2019), and Quirrenbach et al. (2022). Some of these RV detected planets are around mid- and late-M dwarfs, but typically at longer orbital periods than the transiting planets (Schlecker et al. 2022). Due to the heterogeneous nature of this transiting sample, it is not straightforward to estimate the occurrence rate of such planets and compare them to population synthesis models or protoplanetary disk surveys.

So far all of the discoveries of these transiting giant planets have been around early-M dwarfs (M0–M2), which are consistent with the simulations from Burn et al. (2021) that find that gas giants do not form for host stars $<0.5\ M_\odot$. We also note the recent discovery of the interesting TOI-1227 system, which hosts an inflated Jupiter-sized planet orbiting a very young (11 Myr) late-M dwarf ($0.17\ M_\odot$). However, this planet just has a mass upper limit of $0.5\ M_{\rm J}$, is still contracting, and will likely eventually shrink down to a super-Neptune (Mann et al. 2022). Additionally, Parviainen et al. (2021) validated a substellar object orbiting a mid-M dwarf (TOI-519), and placed

Table 3
Summary of Stellar Parameters for TOI-5205

Parameter	Description	Value	References
Main identifiers:			
TOI	TESS Object of Interest	5205	TESS mission
TIC	TESS Input Catalogue	419411415	Stassun
Gaia DR3	⋯	1842656663520849024	Gaia DR3
Equatorial Coordinates and Proper Motion:			
α_{J2016}	R.A. (R.A.)	20:55:04.96	Gaia DR3
δ_{J2016}	decl. (decl.)	+24:21:39.54	Gaia DR3
μ_α	Proper motion (R.A., mas yr^{-1})	41.68 ± 0.02	Gaia DR3
μ_δ	Proper motion (decl., mas yr^{-1})	52.07 ± 0.02	Gaia DR3
ϖ	Parallax (mas)	11.464 ± 0.026	Gaia DR3
d	Distance in parsecs	86.865 ± 0.05	Anders
Broadband photometry:			
G	G mag	14.903 ± 0.003	Gaia DR3
g	PS1 g mag	16.877 ± 0.008	PS1
r	PS1 r mag	15.694 ± 0.008	PS1
i	PS1 i mag	14.21 ± 0.01	PS1
z	PS1 z mag	13.55 ± 0.02	PS1
y	PS1 y mag	13.207 ± 0.005	PS1
J	J mag	11.90 ± 0.02	This work
H	H mag	11.28 ± 0.02	This work
K_s	K_s mag	11.04 ± 0.02	This work
Derived photometry:			
A_G	Extinction in mag	0.12 ± 0.02	Anders
M_G	Absolute G mag	10.09 ± 0.02	Anders
Stellar Parameters:			
$T_{\rm eff}$[a]	Effective temperature in kelvin	3430 ± 54	This work
[Fe/H]	Metallicity	solar	This work
log(g)[a]	Surface gravity in cgs units	4.84 ± 0.03	This work
Sp Type[b]	Spectral Type	M4.0 ± 1.0	This work
R_*[c]	Radius in $R_\odot$	0.394 ± 0.011	This work
M_*[d]	Mass in $M_\odot$	0.392 ± 0.015	This work
L_*	Luminosity in $L_\odot$	0.0194 ± 0.0016	This work
ρ_*	Density in g cm^{-3}	9.0 ± 0.5	This work
Other Stellar Parameters:			
$v \sin i_*$	Rotational velocity in km s^{-1}	<2	This work
ΔRV	Absolute radial velocity in km s^{-1}	-65.9 ± 0.3	This work
U, V, W	Galactic velocities in km s^{-1}	-48.29 ± 0.12, -50.50 ± 0.27, 14.90 ± 0.07	This work
U, V, W[e]	Galactic velocities (LSR) in km s^{-1}	-37.19 ± 0.86, -38.26 ± 0.74, 22.15 ± 0.61	This work

Notes. References are: Stassun (Stassun et al. 2018), Gaia DR3 (Vallenari et al. 2022), PS1 (Evans et al. 2016b), and Anders (Anders et al. 2022).
[a] Using the $T_{\rm eff}$–M_G relation from Rabus et al. (2019).
[b] Spectral typing using relations based on Gaia color (Kiman et al. 2019).
[c] Using R_*–M_K relation from Mann et al. (2015, 2016).
[d] Using M_*–R_* relation from Schweitzer et al. (2019).
[e] The barycentric UVW velocities are converted into local standard of rest (LSR) velocities using the constants from Schönrich et al. (2010).

a 95% upper mass limit of 14 M_J based on Doppler boosting, ellipsoidal variations, etc. TOI-5205b defies this trend, as it orbits a mid-M dwarf host and has one of the largest mass ratios[31] for M-dwarf planets at 0.27%. It is a Jovian-sized planet (Figure 6(a)) with an orbital period of ∼1.6 days (Figure 6(b)), and joins the current sample of ∼10 known transiting gas giants around M dwarfs. TOI-5205b is the first gas giant known to transit a mid-M dwarf, which also results in a transit depth δ of ∼7%. While we do not have precise constraints on the metallicity of the host star, photometric relations estimates suggest a host star metallicity close to solar ([Fe/H] = 0; Appendix A.2).

5.1. Planet Formation

In this section, we present a simple mass budget argument[32] to estimate the minimum mass of the primordial protoplanetary disk in which this giant planet formed under the core-accretion paradigm, where models suggest that runaway gaseous accretion should initiate once a protoplanet has reached a solid core mass of ∼10 $M_\oplus$ (Pollack et al. 1996). We calculate the heavy-element mass for TOI-5205b using the relations from Thorngren et al. (2016) to be ∼60 $M_\oplus$ (or roughly 10× more metal-enriched than the host star), but also note that there is considerable scatter in their sample that can perhaps be attributed to the vagaries in planet formation and evolution.

[31] GJ 3512b has a larger mass ratio at 0.37%, but it does not transit, and hence, only a lower limit of its mass is available (Morales et al. 2019).

[32] Schlecker et al. (2022) discuss some of the other challenges in the formation of gas giants around low-mass M dwarfs under the core-accretion paradigm, beyond the mass budget discussed here.

Table 4
Derived Parameters for the TOI-5205 System

Parameter	Units	Value[a]
Orbital Parameters:		
Orbital Period	P (days)	1.630757 ± 0.000001
Eccentricity	e	$0.020^{+0.020}_{-0.014}$
Argument of Periastron	ω (radians)	$-0.74^{+3.25}_{-1.74}$
Semi-amplitude Velocity	K (m s^{-1})	346 ± 14
Systemic Velocity[b]	$\gamma_{\rm HPF}$ (m s^{-1})	-28 ± 11
RV trend	dv/dt (m s^{-1} yr^{-1})	$0.05^{+4.92}_{-5.08}$
RV jitter	$\sigma_{\rm HPF}$ (m s^{-1})	$14.7^{+16.6}_{-10.1}$
Transit Parameters:		
Transit Midpoint	T_C (BJD$_{\rm TDB}$)	$2459443.47179 \pm 0.00019$
Scaled Radius	R_p/R_*	$0.2720^{+0.0039}_{-0.0043}$
Scaled Semi-major Axis	a/R_*	$10.94^{+0.22}_{-0.21}$
Orbital Inclination	i (degrees)	$88.21^{+0.24}_{-0.22}$
Transit Duration	T_{14} (days)	0.0583 ± 0.0011
Photometric Jitter[c]	$\sigma_{\rm TESS\ S15}$ (ppm)	2985^{+89}_{-85}
	$\sigma_{\rm TESS\ S41}$ (ppm)	4241 ± 50
	$\sigma_{\rm ARCTIC\ 20220422}$ (ppm)	5291 ± 160
	$\sigma_{\rm RBO\ 20220510}$ (ppm)	865^{+947}_{-562}
	$\sigma_{\rm TMMT\ 20220515}$ (ppm)	15759^{+1364}_{-1201}
	$\sigma_{\rm ARCTIC\ 20220703}$ (ppm)	3948^{+472}_{-443}
	$\sigma_{\rm ARCTIC\ 20220717}$ (ppm)	2716 ± 120
Dilution[d,e]	$D_{\rm TESS\ S15}$	0.234 ± 0.012
	$D_{\rm TESS\ S41}$	0.259 ± 0.008
Planetary Parameters:		
Mass	M_p ($M_\oplus$)	343^{+18}_{-17}
	M_p ($M_{\rm J}$)	1.08 ± 0.06
Radius	R_p ($R_\oplus$)	11.6 ± 0.3
	R_p ($R_{\rm J}$)	1.03 ± 0.03
Density	ρ_p (g cm^{-3})	1.21 ± 0.11
Semimajor Axis	a (au)	0.0199 ± 0.0002
Average Incident Flux[f]	$\langle F \rangle$ (10^5 W m^{-2})	0.67 ± 0.06
Planetary Insolation	S ($S_\oplus$)	49 ± 4
Equilibrium Temperature[g]	$T_{\rm eq}$ (K)	737 ± 15

Notes.
[a] The reported values refer to the 16%–50%–84% percentile of the posteriors.
[b] In addition to the "Absolute RV" from Table 3.
[c] Jitter (per observation) added in quadrature to photometric instrument error.
[d] Dilution due to presence of background stars in TESS aperture, not accounted for in the `eleanor` flux.
[e] We treat the dilution terms for RBO 20220510, TMMT 20220515, and ARCTIC 20220717 as nuisance parameters, since those data sets are used only to refine the ephemeris.
[f] We use a solar flux constant = 1360.8 W m^{-2} to convert insolation to incident flux.
[g] We assume the planet to be a blackbody with zero albedo and perfect energy redistribution to estimate the equilibrium temperature.

There are additional uncertainties due to the unknown heavy-element composition, and uncertainties in the equation of state used for their model. As it stands, these models predict $\sim$10 $M_\oplus$ of heavy elements locked up in the central core, with the rest (60–10 $\sim$ 50 $M_\oplus$) diffused in the H/He envelope.

The dust mass of the disk is typically estimated for millimeter-sized dust particles in Class II disks using flux continuum measurements at $\sim$850 μm, which is then used to calculate the mass assuming a blackbody with typical temperatures of 20 K. We decompose the total dust mass in the disk as a product of the disk mass ratio and gas-to-dust ratio (Figure 7). The canonical disk mass scaling (ratio of disk to stellar mass) assumed is $\sim$0.3% based on a study of the Taurus region by Andrews et al. (2013), along with the gas-to-dust ratio of 70–100 ranging from solar to the interstellar medium (ISM; Bohlin et al. 1978). Following these scaling relations suggests a total of 4–5 $M_\oplus$ of dust available for planet formation for TOI-5205, which would be insufficient to form a 10 $M_\oplus$ core to start runaway gaseous accretion even with 100% planet formation efficiency. In this section, we refer to planet formation efficiency as the fraction of the total dust mass of the disk that is used to form TOI-5205b. Therefore in subsequent sections we discuss more realistic scaling values based on recent studies.

5.1.1. Disk Mass Scaling

Pascucci et al. (2016) suggested that the $M_{\rm dust}/M_*$ relation becomes steeper with age, and more so for low-mass stars. If so, these traditional relations would likely underestimate the initial mass of M dwarf disks. Results from Ansdell et al. (2017) agree with this, where they find that (for a given stellar mass) the mass of dust present in a disk tends to decrease with age. They show this using a comparative analysis of disks in five young star-forming regions spanning ages from 1–2 to 5–10 Myr and fitting separate scaling relations to each and then comparing the slopes, thereby corroborating the results from Pascucci et al. (2016). They also note a large dispersion in these scaling relations that are not attributed to measurement systematics, but rather intrinsic astrophysical variation (or diversity) in disk properties within populations.

Observations and simulations based on the Orion Nebula Cluster show that for massive optically thick disks with fluxes >10 mJy (Figure 13 from Eisner et al. 2018), the typical continuum flux–disk mass relations tends to underpredict the disk mass by up to an order of magnitude. However, invoking disk stability arguments, the underestimate is probably less than that because depending on the surface density profile, disks can be $\sim$10% of the stellar mass before they are unstable. These massive optically thick disks (Flux $\sim$10 mJy, $M_{\rm dust} \sim$ 10–100 $M_\oplus$) are seen around M dwarfs as well (Figure 10; Eisner et al. 2018), which is consistent with the typical scatter of $\sim$1 dex seen in these ($M_{\rm disk}/M_*$) relations.

Studies suggest that planet formation is already underway for Class II disks (Greaves & Rice 2010; Najita & Kenyon 2014), and indeed that the primordial disk mass available for giant planet formation early in the disk lifetime (0.1–1 Myr) is likely much larger than the masses measured for Class II disks, also evinced by measurements of the more massive Class I disks (Andrews & Williams 2005; Vorobyov 2011). Additionally, a lot of the solid mass for Class II disks can be locked up in planetesimals and planets, which the millimeter flux measurements would be insensitive to.

Given the significant scatter that exists in these scaling relations, and the various factors that can be responsible for underestimating the primordial dust mass in disks as mentioned above, it is not entirely unreasonable to postulate a more massive disk around TOI-5205 than that predicted

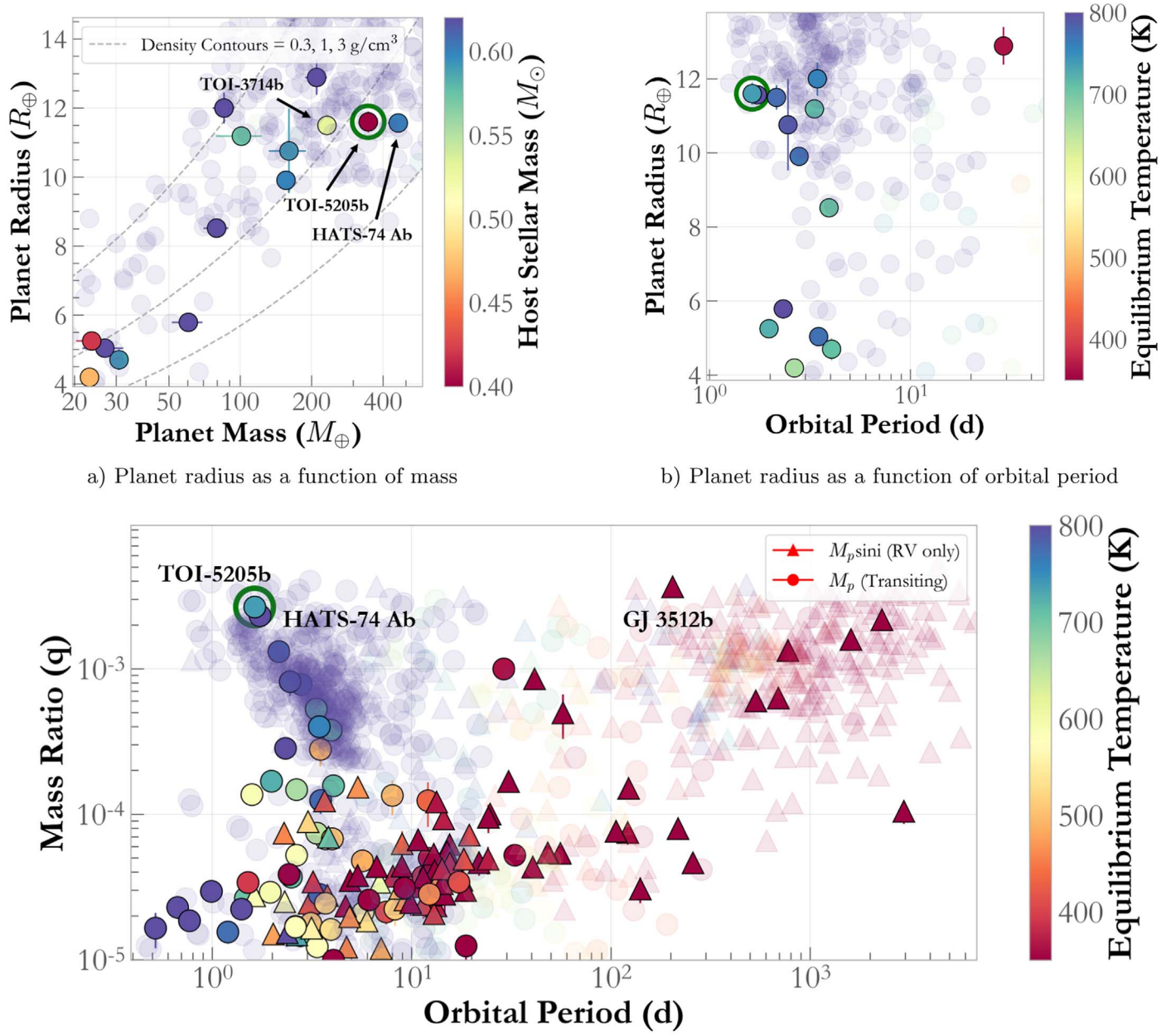

a) Planet radius as a function of mass

b) Planet radius as a function of orbital period

c) Mass ratio as a function of orbital period

Figure 6. (a) We show TOI-5205b (circled in green) in a mass–radius plane alongside other M-dwarf planets (colored by the stellar mass). We also include planets around FGK stars in the background, along with density contours for 0.3, 1, and 3 g cm^{-3} (NASA Exoplanet Archive 2022). (b) The radius–period plane is shown for the same sample of planets, but colored by the equilibrium temperature. (c) Planet-to-star mass ratio vs. orbital period for planets with true mass (transiting; circle) and minimum mass (RV only; triangle) measurements. The planets are color-coded by the equilibrium temperature, the M-dwarf planets are solid, whereas those orbiting FGK stars are shown in the background. TOI-5205b (circled in green) has the highest mass ratio for transiting M-dwarf planets. The highest mass ratio M-dwarf planet is GJ 3512 b at ∼200 days (Morales et al. 2019).

by the standard 0.3% $M_{\rm disk}/M_*$ scaling ratios for Class II disks. In observations pre-Atacama Large Millimeter/submillimeter Array (ALMA; in Taurus; Andrews et al. 2013), and then confirmed with ALMA—Lupus, (Ansdell et al. 2016), Chameleon I (Pascucci et al. 2016), Upper Sco (Barenfeld et al. 2016), and σ Orionis (Ansdell et al. 2017) among others. Indeed Andrews et al. (2013) discussed the presence of outliers in their sample of disks in Taurus, which are anomalously massive at ∼10% total disk-to-stellar mass.

5.1.2. Gas-to-dust Ratio

While the correlation between Jovian planet occurrence and metallicity of the host star has been well established (Gonzalez 1997; Santos et al. 2001; Fischer & Valenti 2005; Ghezzi et al. 2010; Sousa et al. 2011), there is still considerable uncertainty in the gas-to-dust (inverse of metallicity) assumed in planet formation models. This is typically estimated by measuring the mass of the gas in the disk using CO lines, which is then combined with dust mass measurements from mm continuum to obtain the gas-to-dust mass ratio.

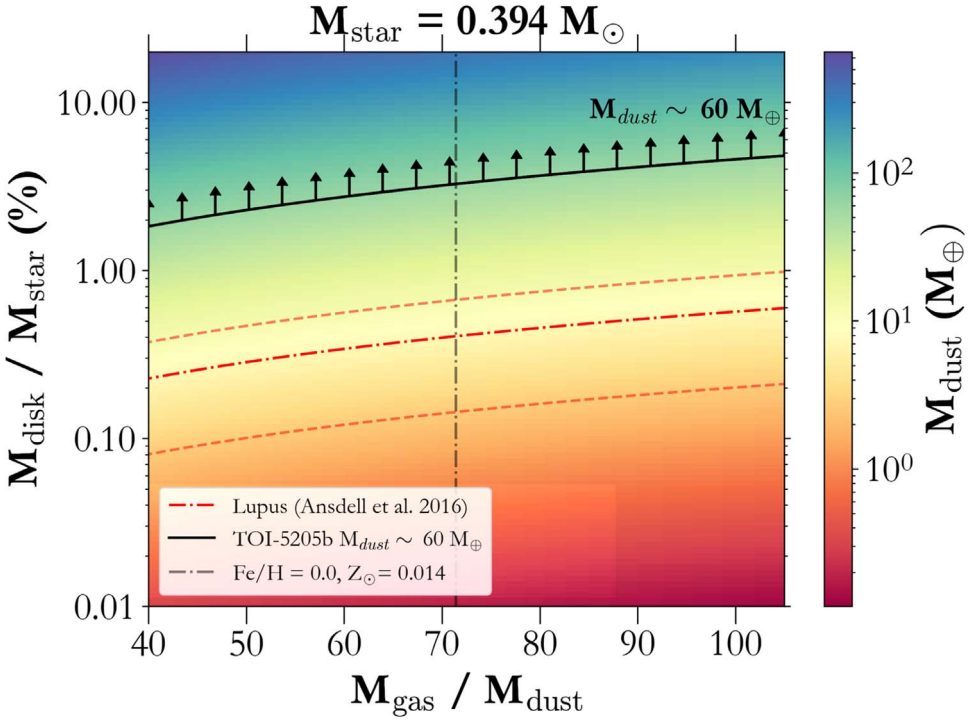

Figure 7. The mass budget of the dust present in the disk as a function of disk mass ratio (disk to star; *y*-axis), and the gas-to-dust ratio (*x*-axis). The black line is the contour corresponding to the estimated heavy-element mass for TOI-5205b of ∼60 $M_\oplus$ based on relations from Thorngren et al. (2016). This indicates the disk properties required to form the planet even at 100% formation efficiency, i.e., if all of the dust present in the disk could accumulate in TOI-5205b. A lower formation efficiency would imply an even larger disk dust mass. The red line shows the dust mass for a disk orbiting a mid-M dwarf as massive as TOI-5205 using the scaling relations from Ansdell et al. (2016) in the young (1–3 Myr) Lupus complex, while the region next to it shows the 1σ uncertainty. We also include a vertical line to show solar metallicity of $Z_\odot = 0.014$, or a gas-to-dust ratio of ∼71. The heavy-element core for TOI-5205b (black line) is *much* more massive than expected from scaling relations based on the Lupus complex.

The typical ISM estimate for the gas-to-dust ratio is ∼100 (Bohlin et al. 1978), but a small sample of Taurus disks revealed a mean value closer to ∼16 (Williams & Best 2014). In fact, Ansdell et al. (2016) found that for disks in Lupus, the ratio might even be closer to 10, which was then corroborated by Miotello et al. (2017). While these CO measurements could indicate a low gas-to-dust ratio, they could also be due to the selective loss of CO gas in the disk due to CO condensation, which would not apply to H_2. The latter was supported by Rosotti et al. (2017), who showed that the accretion rate versus disk mass relationship is consistent when the mass of the disk is estimated using a gas-to-dust ratio of ∼100. Based on this they suggest that this ratio cannot be lower than by a factor of 2 from the canonical ISM value of 100. Most recently, Anderson et al. (2022) found that gas mass measurements of CO isotopologues extrapolated to H_2 can have significant uncertainties, often by many orders of magnitude, thereby severely underestimating the gas-to-dust ratio. All of this is to suggest that while the intrinsic gas-to-dust ratio for protoplanetary disks is hard to constrain, it should be within a factor of few of 100.

For a solar metallicity $Z_\odot = 0.014$ disk (gas-to-dust ratio of ∼70), we would require a disk that is about 3% total disk-to-stellar mass, to have the ∼60 $M_\oplus$ of heavy elements estimated for TOI-5205b. While a detailed planet formation simulation is beyond the scope of this paper, Lin et al. (2018) suggested a maximum efficiency for giant planet formation under pebble accretion of ∼10%, which would require a disk that is ∼30% in host star mass. Conversely, if the actual heavy-element mass for TOI-5205b is lower than predicted by Thorngren et al. (2016) model, the required disk mass would scale down by the same factor.

5.1.3. Disk Lifetimes (Increasing Efficiency of Planet Formation)

Apart from the low disk masses, the other issue with giant planet formation around M dwarfs is the longer orbital timescales (at a given separation) due to the lower host star mass. This results in a much slower growth rate for planetesimal formation (∼1 Myr), which must succeed in forming a massive enough core to initiate runaway accretion before the disk disperses.

The typical disk lifetime inferred by studying the incidence of disks in a cluster of different ages is ∼3 Myr, with an upper bound of ∼10 Myr (Ribas et al. 2014). It has also been established that this lifetime scales with stellar mass, and while the disks around M dwarfs typically last longer (Carpenter et al. 2006), they still disperse within ∼20 Myr (Pecaut & Mamajek 2016). Recently the discovery of very long-lived ($\gtrsim$20 Myr), so called "Peter Pan" disks has been reported around M dwarfs (Lee et al. 2020; Silverberg et al. 2020; Gaidos et al. 2022). Models suggest that the existence of these disks requires relatively high disk masses and very low external photoevaporation, similar to those found at the periphery of star-forming regions (Coleman & Haworth 2020). These longer-lived massive disks would offer more time for the formation of solid cores massive enough to initiate runaway gas accretion under the slower core-accretion paradigm.

5.1.4. Disk Instability Scenario

Previous studies use the positive correlation for giant plant occurrence with stellar mass and metallicity (Gonzalez 1997; Santos et al. 2001; Fischer & Valenti 2005; Ghezzi et al. 2010; Sousa et al. 2011) as evidence of core accretion

(Ida & Lin 2005; Thorngren et al. 2016; Ghezzi et al. 2018). However, this correlation with metallicity is only seen for $M_p \lesssim 4\ M_J$, while stars hosting more massive planets are on average closer to solar metallicity, or even metal-poor (Santos et al. 2017; Schlaufman 2018; Maldonado et al. 2019). This suggests a dichotomy in the formation mechanism centered at $\sim$4 M_J, with less-massive objects classified as planets formed through core accretion, while more-massive planets form through disk instability, similar to brown dwarfs and low-mass stars (Schlaufman 2018).

Even though the mass of TOI-5205b is $<4\ M_J$, due to the large mass ratio for TOI-5205b, we consider the disk instability scenario. Interestingly enough, this $\sim$10% disk mass regime discussed in the previous section is also the typical disk mass required to enable giant planet formation under the disk instability scenario either close-in (Boss 2006) or farther out (Boss 2011). Disk instability has been proposed as a faster ($\sim 10^3$ yr) alternative to the slower ($\sim$1 Myr) core-accretion formation scenario for M dwarfs where the lower host star mass translates to longer orbital timescales at a given distance from the star (Laughlin et al. 2004). Under this mechanism, a massive 10%–20% disk would have to be marginally unstable to start breaking up into lumps of gas and dust. These instabilities typically also require cooler temperatures, which warrants the formation of the planet at large orbital separations (ex situ formation[33]), followed by subsequent inward migration through disk migration (Kley & Nelson 2012) or high-eccentricity excitation (Beaugé & Nesvorný 2012). Given the scope of current models, we cannot rule out disk instability as a potential formation mechanism for TOI-5205b.

Overall, we see two possible ways to explain the existence of this planet given current theories of planet formation—(i) A $\sim$60 $M_\oplus$ solid heavy-element core: which would require a disk that is $\sim$3%–30% the mass of the host star (for 100% and 10% formation efficiency, respectively), under which case both core-accretion and disk instability scenarios should be possible. (ii) The interior models are biased and overpredict the solid core mass. Under the canonical core accretion scenario, this would suggest a core of 10 $M_\oplus$, and would need a disk that is $\sim$0.5%–5% the mass of the host star (for 100% and 10% formation efficiency, respectively).

5.2. Atmospheric Characterization

Characterizing the atmosphere of TOI-5205b may provide clues needed to differentiate between formation mechanisms. Did it form via disk instability or core accretion, furthermore, under core accretion, did it form in situ or farther out and then migrate inward through disk or disk-free migration?

Assuming formation via core accretion, TOI-5205b is expected to have a superstellar metallicity if it underwent disk migration, or either sub- or superstellar metallicity if it underwent disk-free migration (Madhusudhan et al. 2014). If TOI-5205b is metal-enriched, and therefore likely formed via core accretion, the second question surrounds whether TOI-5205b formed in situ or farther out before migrating inward. Multiple studies suggest that C/O ratios could provide some indication as to whether a planet formed inside or beyond various disk snowlines (e.g., Öberg et al. 2011; Madhusudhan et al. 2014). As molecules "freeze-out," they remove those elements from the overall gas composition. When water freezes, for example, it removes some of the overall oxygen from the gas increasing the C/O ratio beyond the water-ice line (Öberg et al. 2011). Similarly, Knierim et al. (2022) showed that the ratio of refractory and volatile elements can depend on the migration history of the planet. While Dash et al. (2022) emphasized there are degeneracies and assumptions that must be considered, such as post-formation bombardment, or sublimation of the core, C/O ratios may provide the first insights into where TOI-5205b originally formed.

Under the disk instability hypothesis, TOI-5205b would have formed from a collapse of a massive region of the protoplanetary disk prior to migrating inward. Therefore, from a first approximation, it is assumed that its atmosphere should reflect that of the protoplanetary disk and its host star—i.e., should have the same metallicity and abundances as TOI-5205 (e.g., Helled & Bodenheimer 2010; Helled & Lunine 2014). However, recent works demonstrate that this initial picture may become complicated both by location of the initial collapse (Madhusudhan et al. 2014) or size of particles/objects accreted during this process (Helled et al. 2014). Hobbs et al. (2022) suggested that comparing abundances of various molecules, notably methane, carbon monoxide/dioxide, and hydrogen cyanide, may be a useful method for distinguishing the two formation pathways. Even with these complications, discovering a solar or near-solar metallicity atmosphere (heavy-element abundance of $\sim$1%) for TOI-5205b would hint at the potential for gravitational instability. In this scenario, the heavy-element mass estimated using the Thorngren et al. (2016) sample would be incorrect for TOI-5205b.

TOI-5205b is a compelling target scientifically, and with its 7% transit depth, it is also an object easily accessible with James Webb Space Telescope (JWST) observations. Even though it is a relatively cool (740 K) Jovian world, it still possesses a large transmission spectroscopy metric (TSM) of $\sim$100 placing it in the second quartile of their giant planet sample (assuming a scale factor of 1.15) from Kempton et al. (2018). TOI-5205b also has one of the largest emission spectroscopy metrics (ESM) of any planet at $\sim$150, in part due to its R_p/R_s and also its bright mid-M dwarf host (Figure 8).

We calculate model transmission and thermal emission spectra assuming 1×, 10×, and 100× solar metallicity. We then simulate JWST NIRSpec PRISM data using `PandExo` (Batalha et al. 2017) corresponding to the 1× solar cases, assuming two transits/secondary eclipses, respectively. The transmission spectra are calculated using `Exo-Transmit` (Kempton et al. 2017). We predict that NIRSpec should significantly distinguish between each of the model transmission spectra, as a result of the smaller spectral feature amplitudes for the 100× solar metallicity model and the onset of a CO_2 feature in the 4–5 μm range between the 1× and 10× solar metallicity models. The model thermal emission spectra are generated using the self-consistent atmospheric model `GENESIS` (Gandhi & Madhusudhan 2017, 2019; Piette & Madhusudhan 2020; Piette et al. 2020). `GENESIS` calculates full line-by-line radiative transfer under the assumptions of radiative-convective equilibrium, hydrostatic equilibrium, and thermochemical equilibrium. Here, chemical equilibrium abundances are calculated using the analytic prescription of Heng & Tsai (2016). We include opacity due to H_2O, CH_4, NH_3, HCN, CO, CO_2, C_2H_2, and collision-induced absorption (CIA) due to H_2–H_2 and H_2–He. The absorption cross sections

[33] See Helled et al. (2014), Dawson & Johnson (2018), and Helled (2021) for comprehensive reviews on giant planet formation.

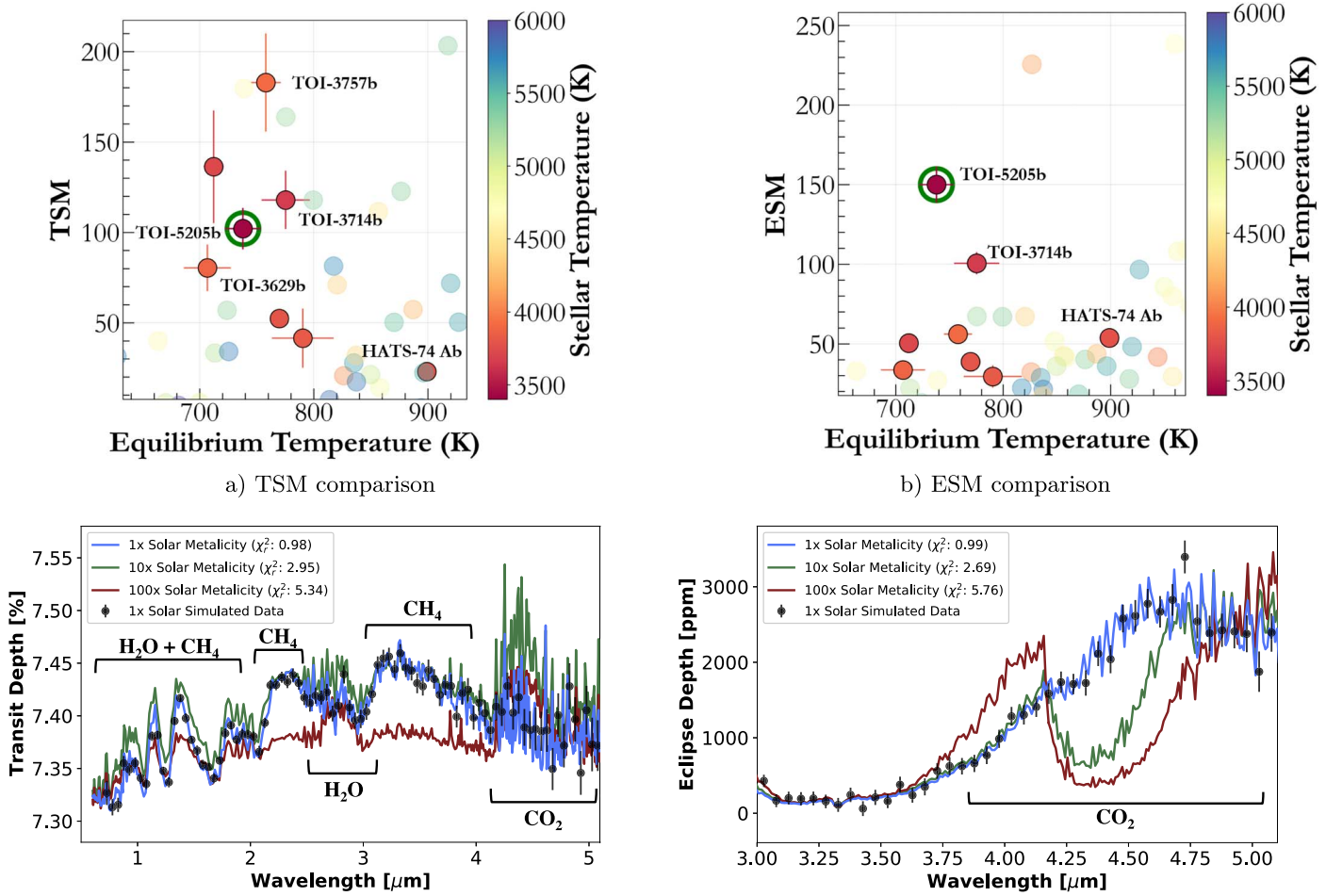

Figure 8. (a)–(b) We show the TSM and ESM for TOI-5205b with respect to other M dwarf gas giants, $R_p > 8\ R_\oplus$ (solid), while those orbiting FGK stars are in the background. TOI-5205b (circled in green) has a high TSM (∼100) and ESM (∼150) that make it an excellent target for atmospheric characterization to estimate the chemical composition of the planet. (c)–(d) Simulated transmission and thermal emission spectra for three different atmospheric metallicities, along with `PandExo` predictions for JWST NIRSPEC PRISM spectra for two transits and eclipses, respectively.

for these species are calculated using the methods described in Gandhi & Madhusudhan (2017), using data from ExoMol, HITEMP, and HITRAN (H_2O, CO, and CO_2: Rothman et al. 2010; CH_4: Yurchenko et al. 2013; Yurchenko & Tennyson 2014; NH_3: Yurchenko et al. 2011; HCN: Harris et al. 2006; Barber et al. 2014; C_2H_2: Rothman et al. 2013; CIA: Richard et al. 2012). As shown in Figure 8, the 1×, 10×, and 100× solar metallicity models are easily distinguishable in the ∼4–5 μm range due to the onset of an increasingly deep CO_2 feature as metallicity increases. Atmospheric characterization of TOI-5205b with both transmission and thermal emission spectroscopy is therefore a promising avenue to characterize its atmospheric metallicity and C/O ratio, and to place constraints on its formation and evolution.

6. Summary

We present the discovery of TOI-5205b, a Jovian exoplanet orbiting a solar metallicity mid-M dwarf. TOI-5205b was first identified from TESS photometry, and then characterized using a combination of ground-based photometry, RVs, spectroscopic observations, and speckle imaging.

The large mass ratio of the planet (∼0.3%) necessitates a disk that is ∼10% as massive as the host star, thereby stretching our current understanding of protoplanetary disks around M dwarfs. The typical scaling relations used to estimate disk properties are hard-pressed to reproduce the primordial disks that are massive enough to form such a planet. However there is significant scatter in disk dust mass measurements and scaling relations, which could still explain such massive planets around mid-M dwarfs.

TOI-5205b has a large transit depth of 7%, which makes it an excellent candidate for transmission and emission spectroscopy, both from the ground (high-resolution) and space (JWST). Atmospheric characterization could help constrain the metallicity of the planet and could offer clues about their formation history.

The large sample of M dwarfs being observed by TESS is already improving our understanding of planet formation around M dwarfs. While the first few discoveries were limited to the early-M dwarfs, we are now starting to find that it is indeed possible to form these gas giants around mid-M dwarfs. As we go from a sample of these planets around solar-type stars to mid-M dwarfs, there is a unique opportunity to study planet

formation at its extremes, spanning more than a 2× range in stellar mass, and 100× in luminosity!

We thank the anonymous referee for the valuable feedback, which has improved the quality of this manuscript.

S.K. thanks Rocio Kiman for help with spectral typing using Gaia colors; Alycia J. Weinberger for illuminating discussions and references regarding protoplanetary disks around M dwarfs; and Peter Gao for discussions regarding the atmospheric characterization of these planets and for proofreading sections of this manuscript. S.K. acknowledges research support from Carnegie Institution of Science through the Carnegie Fellowship.

The Pennsylvania State University campuses are located on the original homelands of the Erie, Haudenosaunee (Seneca, Cayuga, Onondaga, Oneida, Mohawk, and Tuscarora), Lenape (Delaware Nation, Delaware Tribe, Stockbridge-Munsee), Shawnee (Absentee, Eastern, and Oklahoma), Susquehannock, and Wahzhazhe (Osage) Nations. As a land grant institution, we acknowledge and honor the traditional caretakers of these lands and strive to understand and model their responsible stewardship. We also acknowledge the longer history of these lands and our place in that history.

These results are based on observations obtained with the Habitable-zone Planet Finder Spectrograph on the HET. We acknowledge support from NSF grants AST-1006676, AST-1126413, AST-1310885, AST-1310875, ATI 2009889, ATI-2009982, AST-2108512, AST-2108801 and the NASA Astrobiology Institute (NNA09DA76A) in the pursuit of precision RVs in the NIR. The HPF team also acknowledges support from the Heising-Simons Foundation via grant 2017-0494. The Low Resolution Spectrograph 2 (LRS2) was developed and funded by the University of Texas at Austin McDonald Observatory and Department of Astronomy and by Pennsylvania State University. We thank the Leibniz-Institut für Astrophysik Potsdam (AIP) and the Institut für Astrophysik Göttingen (IAG) for their contributions to the construction of the integral field units. The Hobby-Eberly Telescope is a joint project of the University of Texas at Austin, the Pennsylvania State University, Ludwig-Maximilians-Universität München, and Georg-August Universität Gottingen. The HET is named in honor of its principal benefactors, William P. Hobby and Robert E. Eberly. The HET collaboration acknowledges the support and resources from the Texas Advanced Computing Center. We thank the Resident astronomers and Telescope Operators at the HET for the skillful execution of our observations with HPF. We would like to acknowledge that the HET is built on Indigenous land. Moreover, we would like to acknowledge and pay our respects to the Carrizo & Comecrudo, Coahuiltecan, Caddo, Tonkawa, Comanche, Lipan Apache, Alabama-Coushatta, Kickapoo, Tigua Pueblo, and all of the American Indian and Indigenous Peoples and communities who have been or have become a part of these lands and territories in Texas, here on Turtle Island.

We acknowledge support from NSF grants AST-1910954, AST-1907622, AST-1909506, and AST-1909682 for the ultra-precise photometry effort.

The Low Resolution Spectrograph 2 (LRS2) was developed and funded by the University of Texas at Austin McDonald Observatory and Department of Astronomy and by Pennsylvania State University. We thank the Leibniz-Institut für Astrophysik Potsdam (AIP) and the Institut für Astrophysik Göttingen (IAG) for their contributions to the construction of the integral field units.

WIYN is a joint facility of the University of Wisconsin-Madison, Indiana University, NSF's NOIRLab, the Pennsylvania State University, Purdue University, University of California-Irvine, and the University of Missouri. The authors are honored to be permitted to conduct astronomical research on Iolkam Du'ag (Kitt Peak), a mountain with particular significance to the Tohono O'odham. Data presented herein were obtained at the WIYN Observatory from telescope time allocated to NN-EXPLORE through the scientific partnership of NASA, the NSF, and NOIRLab.

The authors extend deepest gratitude to Zade Arnold, Joe Davis, Michelle Edwards, John Ehret, Tina Juan, Brian Pisarek, Aaron Rowe, Fred Wortman, the Eastern Area Incident Management Team, and all of the firefighters and air support crew who fought the recent Contreras fire. Against great odds, you saved Kitt Peak National Observatory.

Some of the observations in this paper made use of the NN-EXPLORE Exoplanet and Stellar Speckle Imager (NESSI). NESSI was funded by the NASA Exoplanet Exploration Program and the NASA Ames Research Center. NESSI was built at the Ames Research Center by Steve B. Howell, Nic Scott, Elliott P. Horch, and Emmett Quigley.

This work has made use of data from the European Space Agency (ESA) mission Gaia (https://www.cosmos.esa.int/gaia), processed by the Gaia Data Processing and Analysis Consortium (DPAC, https://www.cosmos.esa.int/web/gaia/dpac/consortium). Funding for the DPAC has been provided by national institutions, in particular the institutions participating in the Gaia Multilateral Agreement.

Computations for this research were performed on the Pennsylvania State University's Institute for Computational and Data Sciences Advanced CyberInfrastructure (ICDS-ACI). This content is solely the responsibility of the authors and does not necessarily represent the views of the Institute for Computational and Data Sciences.

We acknowledge support from NSF grant AST-1907622 in the pursuit of precise photometric observations from the ground.

The Center for Exoplanets and Habitable Worlds is supported by the Pennsylvania State University, the Eberly College of Science, and the Pennsylvania Space Grant Consortium.

Some of the data presented in this paper were obtained from MAST at STScI. Support for MAST for non-HST data is provided by the NASA Office of Space Science via grant NNX09AF08G and by other grants and contracts. This work includes data collected by the TESS mission, which are publicly available from MAST. Funding for the TESS mission is provided by the NASA Science Mission directorate. This research made use of the (i) NASA Exoplanet Archive, which is operated by Caltech, under contract with NASA under the Exoplanet Exploration Program, (ii) SIMBAD database, operated at CDS, Strasbourg, France, (iii) NASA's Astrophysics Data System Bibliographic Services, and (iv) data from 2MASS, a joint project of the University of Massachusetts and IPAC at Caltech, funded by NASA and the NSF.

This research has made use of the SIMBAD database, operated at CDS, Strasbourg, France, and NASA's Astrophysics Data System Bibliographic Services.

This research has made use of the Exoplanet Follow-up Observation Program website, which is operated by the California Institute of Technology, under contract with the National Aeronautics and Space Administration under the Exoplanet Exploration Program.

The research was carried out (in part) at the Jet Propulsion Laboratory, California Institute of Technology, under a contract with the National Aeronautics and Space Administration (NASA).

C.I.C. acknowledges support by an appointment to the NASA Postdoctoral Program at the Goddard Space Flight Center, administered by USRA through a contract with NASA.

S.K. would like to acknowledge Theodora and Rafa for help with this project.

This research made use of exoplanet (Foreman-Mackey et al. 2021a, 2021b) and its dependencies (Kipping 2013; Robitaille et al. 2013; Salvatier et al. 2016; The Theano Development Team et al. 2016; Foreman-Mackey et al. 2017; Astropy Collaboration et al. 2018; Foreman-Mackey 2018; Kumar et al. 2019; Luger et al. 2019; Agol et al. 2020).

Facilities: Gaia, HET (HPF), APO (ARCTIC), WIYN 3.5 m (NESSI), Magellan (FourStar) RBO TESS, Exoplanet Archive.

Software: `ArviZ` (Kumar et al. 2019), AstroImageJ (Collins et al. 2017), `astroquery` (Ginsburg et al. 2019), `astropy` (Robitaille et al. 2013; Astropy Collaboration et al. 2018), `barycorrpy` (Kanodia & Wright 2018), `celerite2` (Foreman-Mackey et al. 2017; Foreman-Mackey 2018), `daophot` (Stetson 1987; Stetson & Harris 1988), `eleanor` (Feinstein et al. 2019), `exoplanet` (Foreman-Mackey et al. 2021a, 2021b), `Exo-Transmit` Kempton et al. (2017), `GENESIS` (Gandhi & Madhusudhan 2017), `HxRGproc` (Ninan et al. 2018), `ipython` (Pérez & Granger 2007), `lightkurve` (Lightkurve Collaboration et al. 2018), `matplotlib` (Hunter 2007), `numpy` (Harris et al. 2020; Oliphant 2006), `Panacea`,[34] `pandas` (McKinney 2010), `PandExo` (Batalha et al. 2017), `PyMC3` (Salvatier et al. 2016), `pyHammer` (Roulston et al. 2020), `scipy` (Oliphant 2007; Virtanen et al. 2020), `SERVAL` (Zechmeister et al. 2018), `starry` (Luger et al. 2019; Agol et al. 2020), `Theano` (The Theano Development Team et al. 2016).

Appendix
Stellar Characterization

A.1. Spectral Classification

1. Template Matching (`pyHammer`): We classify the spectral subtype for TOI-5205 with the LRS2 spectra using `pyHammer` (Roulston et al. 2020), which is based on `The Hammer` (Covey et al. 2007), and uses an empirical template averaged across many observations. The empirical template is derived from the MaNGA Stellar Library (MaStar), which consists of well-calibrated optical spectra from SDSS IV (Yan et al. 2019). The relative calibration for this template is accurate to $<5\%$, spanning stellar spectral types and metallicity. After applying the response and telluric correction, the combined LRS2 spectra (blue + red) matches a metal-rich M5 spectra the best (based on spectral indices; Roulston et al. 2020), and also gives the lowest residuals when comparing the entire spectra (Figure 9).
2. Spectral ratios: We also use the spectral ratios defined by Kirkpatrick et al. (1991) surrounding CaH, Ti I, Na I, and Ca II, to obtain a spectral type of M3–M4.5 based on the LRS2 spectra.
3. Photometry relations: We also use relations from Kiman et al. (2019) to obtain a spectral type using the absolute G magnitude, which suggests an $\sim$M3.5 spectral type. Using the $G-J$ relation from Figure 13 in Cifuentes et al. (2020) corroborates the M4 spectral type estimate for the given $G-J$ color of $\sim$3.

Considering the results from the template-matching (M5) and color relations, we adopt a spectral classification of M4.0 to which we ascribe an error of 1.0 subtype.

A.2. Using Photometric Relations

We obtain M_G of $10.09^{+0.01}_{-0.03}$ from Anders et al. (2022), which takes into account extinction using estimates from multiple photometric surveys. Using Equation (11) from Rabus et al. (2019), we estimate a $T_{\rm eff}$ from M_G of 3430 K with an error of 54 K, where we propagate the error in M_G to $T_{\rm eff}$ and combining in quadrature with the scatter in the polynomial fit. We do note that our $T_{\rm eff}$ estimate is on the hotter end of that expected for an M4 spectral type; however, this is not too surprising given the uncertainty of 1 spectral type, and the considerable scatter in theoretical models for mid-type M dwarfs.

We use the empirically calibrated polynomial relations derived by Mann et al. (2015) to estimate the stellar radius. Given the large scatter in the $T_{\rm eff}$ versus stellar radius relation (Figure 9 from Mann et al. 2015), we use the absolute K_s magnitude–stellar radius relation instead, and adopt an error of $\sim$3% on the stellar radius based on their cross-validation results. The full transit obtained for TOI-5205b from the 3.5 m APO telescope on 2022 July 16 is used to obtain a density constraint on the star of 8.8 ± 0.4 g cm^{-3}, which is also consistent with the $\sim$0.39 $R_\odot$ obtained above. We also use M_G along with the bolometric calculator[35] for the given $T_{\rm eff}$ (Creevey et al. 2022), to obtain the bolometric magnitude, luminosity, and subsequently a stellar radius of $\sim 0.37 \pm 0.02$ $R_\odot$, which is consistent with our radius estimate using the relations from Mann et al. (2015).

Finally, we use the Stefan–Boltzmann law to obtain a stellar luminosity, and the empirically calibrated M–R relationship for main-sequence M dwarfs (Equation (6); Schweitzer et al. 2019) to obtain a stellar mass (Table 3). We also verify the stellar mass using photometric relations from Henry & McCarthy (1993), Delfosse et al. (2000), Benedict et al. (2016), and Mann et al. (2019) and consistently obtain similar results to $\sim 1\sigma$–2σ. Mass–luminosity relations in the optical (M_V) from Henry & McCarthy (1993) and Benedict et al. (2016) give discrepant results with the M_K mag relations due to the effect of the TiO and VO molecules, especially below 0.4 $M_\odot$ as discussed by Baraffe et al. (1998).

Photometric relations from Bonfils et al. (2005), Schlaufman & Laughlin (2010), and Neves et al. (2012) give metallicities of 0.02, 0.19, and 0.09 dex, respectively, along with a typical uncertainty of 0.2 dex. Maldonado et al. (2020) noted that

[34] https://github.com/grzeimann/Panacea

[35] https://www.cosmos.esa.int/web/gaia/dr3-bolometric-correction-tool

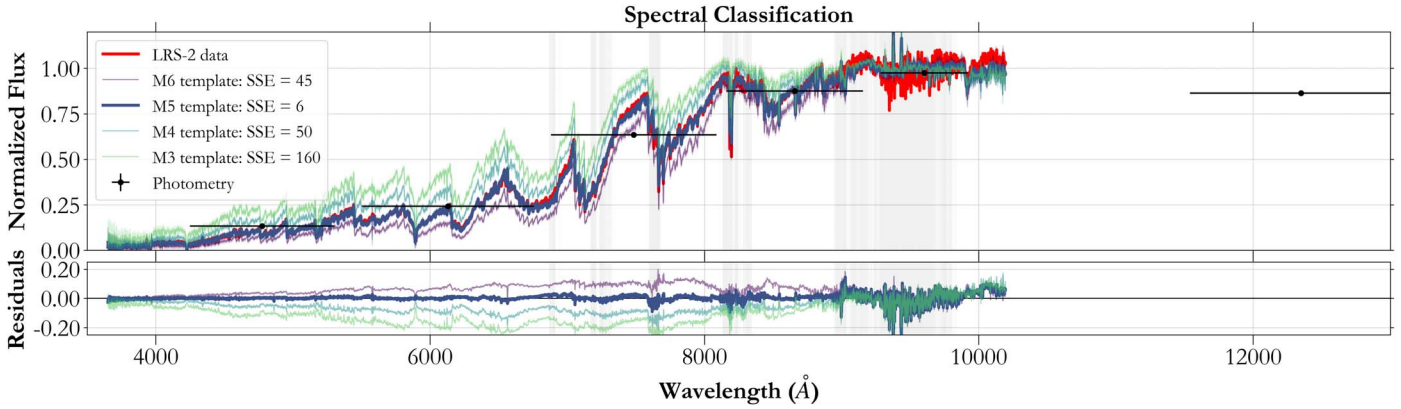

Figure 9. Comparing the LRS2 spectra with the empirical templates from `pyHammer`. In red we show the observed LRS2 spectra after response and telluric correction, while empirical templates from M3 to M6 are shown in different colors, while the vertical lines in the background denote the regions of significant telluric absorption. The increased noise (∼5%) in the measured spectrum around ∼9000 Å can be attributed to the telluric correction. We include the residuals in the lower plot and also the summed square errors (SSE) in the legend showing that the M5 template is the preferred one. We also plot the normalized fluxes based on the photometric magnitudes from PS1 (optical) and the *J* magnitude from FourStar with the horizontal error bar depicting the bandpass. We do not include the *H*, *K* magnitudes from FourStar in this plot to focus on the optical spectra and template comparison.

photometric metallicities have systematically lower values than corresponding spectroscopic techniques. However due to the sparse sampling of the `SpecMatch-Emp` library in $T_{\rm eff}$–[Fe/H] plane for mid-M dwarfs (Yee et al. 2017), and the potential covariance between these two quantities, we do not have reliable metallicity estimates from `SpecMatch-Emp` for this mid-M dwarf. Instead, we adopt a qualitative estimate of solar metallicity for TOI-5205 (Table 3). See Passegger et al. (2022) for a detailed discussion of the complexities in metallicity determination for M dwarfs.

A.3. Estimating Activity Level

A.3.1. Using Hα from LRS2 Spectra

Emission in the Hα line compared to the overall stellar bolometric luminosity is a powerful stellar activity indicator for M dwarfs (West et al. 2015). To estimate $\log(L_{\rm H\alpha}/L_{\rm bol})$ for TOI-5205, we measured the pseudo-equivalent width of the Hα line from the LRS-2 red channel spectrum. Prior to measuring pEW(Hα), we shifted the spectra to zero radial velocity, accounting for the barycentric velocity and absolute velocity of the star. We measure the pEW(Hα) using the following equation:

$$\mathrm{pEW(H}\alpha) = \int_{\lambda_1}^{\lambda_2}\left(1 - \frac{F(\lambda)}{F_{\rm pc}}\right)d\lambda \tag{A1}$$

where we integrate over the limit from $\lambda_1 = 6560$ Å and $\lambda_2 = 6566\,\mathring{A}$. $F_{\rm pc}$ is the average of the median flux in the pseudo-continuum in the ranges from 6545–6559 Å, and 6567 −6580 Å after removing a linear slope fit to that range seen in the pseudo-continuum surrounding the Hα line for late-M dwarfs. In doing so, we measure a $\mathrm{pEW(H}\alpha) = -0.81 \pm 0.01$ Å, where the error is the statistical uncertainty accounting for the S/N of the observed spectrum.

To estimate $\log(L_{\rm H\alpha}/L_{\rm bol})$, we use the following equation:

$$\log\left(\frac{L_{\rm H\alpha}}{L_{\rm bol}}\right) = \log\chi + \log(-\mathrm{pEW(H}\alpha)), \tag{A2}$$

where $\log\chi$ is the ratio of the flux in the continuum near Hα to the bolometric flux. We use the estimate χ following the methodology in Reiners & Basri (2008), which gives χ as a function of stellar effective temperature for M dwarfs stars. In doing so, we obtain a $\log(\chi) = -4.3$, and $\log(L_{\rm H\alpha}/L_{\rm bol}) = -4.4$. From the sample of $\log(L_{\rm H\alpha}/L_{\rm bol})$ values in West et al. (2015), this value for TOI-5205 is suggestive of an M4 star that is not highly active.

A.3.2. Rotation Period Estimates

In Section 4, we describe the fitting of the TESS photometry from sectors 15 and 41 with separate stellar rotation kernels that return a rotation period of $3.7^{+1.3}_{-1.1}$ days from sector 15 and 4.3 ± 0.6 days from sector 41. The kernel consists of two simple harmonic oscillator terms—one at the rotation period, with the second one at half the period. This observed period is also seen as a peak in a generalized Lomb–Scargle (GLS) periodogram (Lomb 1976; Scargle 1982; Zechmeister & Kürster 2009) on the sector 41 photometry (after masking the transits of TOI-5205b) using its `astropy` implementation, and a significant peak (20% false-alarm probability) is found at ∼4.4 days.

However, similar to TOI-3757 b (Kanodia et al. 2022), we see that this periodic signal is likely an artifact from the photometry reduction of the FFI. The signal is seen a few adjoining pixels in an 8×8 grid centered on the centroid for TOI-5205, which suggests that the signal is not astrophysical in origin. This is further corroborated by the lack of detected rotational broadening in the HPF spectra, with which we can place a limit of $v \sin i < 2$ km s^{-1} on the host star. The corresponding equatorial velocity for a ∼4.4 days rotation period would be ∼3.7 km s^{-1}. Furthermore, we also check the publicly available data from ASAS-SN (Kochanek et al. 2017) in *V* and *g*, and ATLAS (Tonry et al. 2018) in the cyan (420–650 nm) and orange (560–820 nm) bands using a GLS periodogram, and do not find any significant signals. We did not find any publicly available data from the Zwicky Transient Facility Data Release 12 (Masci et al. 2019).

Based on the Hα equivalent width estimate and lack of detectable photometric rotation signal for TOI-5205, we classify TOI-5205 as an inactive, old star.

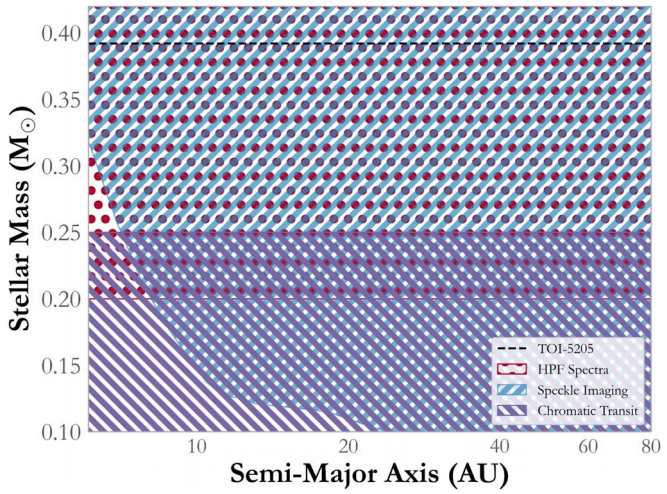

Figure 10. We show the limits placed on a blended secondary companion using three different methods. In blue (forward leaning lines) we show the constraints from speckle imaging (Section 2.4). In purple (backward leaning lines) we show the limits from comparing transit depths in g' and i' (Appendix A.4.2). Given the short-observing baseline of the HPF RVs, the RV slope can only rule out massive companions with periods <40 days (0.2 au), which are not shown here. Instead, the flux constraint from HPF spectra (red dots) order 5 (∼8700 Å) is used to rule out stars more massive than 0.2 $M_\odot$ within the HPF aperture (0.″85 radius ∼80 au) as long as they have velocity offsets $|\Delta v| > 5$ km s^{-1}. The dashed black line is the mass of the primary—TOI-5205.

A.4. Blended Sources of Contamination

The stellar density estimated assuming a circular orbit (8.8 ± 0.4 g cm^{-3}) confirms the mid-M dwarf spectral type for the host (Appendix A.2). This also rules out the background eclipsing binary scenario around distant giant stars.

The speckle imaging from NESSI is used to resolve the presence of any objects down to a separation of 0.″3 or about 27 au (Figure 10). We then attempt to place constraints on unresolved stellar companions using HPF spectra, Gaia astrometry, archival imaging, photometry, and the RVs.

A.4.1. Background Objects

We look for background companions by comparing our observations of TOI-5205 from ARCTIC on 2022 April 22 (Section 2.2.1) with observations from the Palomar Observatory Sky Survey (POSS-1; Harrington 1952; Minkowski & Abell 1963) image taken on 1954 June 28. The POSS-1 plate images were taken with Eastman 103a-O spectroscopic plates without a filter and have a limiting magnitude of ∼20. Over this period, TOI-5205 has had a proper motion of ∼4.″5, which is comparable to the PSF FWHM for the POSS-1 photographic plate observations. These archival observations rules out background companions that might be blended with TOI-5205 with a contrast of $\Delta V \sim 4$.

The closest companion seen in both images is TIC 1951446034, which is a resolved background star that is ∼4″ away and not comoving.

A.4.2. Comoving Objects

We rule out the possibility of a system where TOI-5205b transits the primary, but is accompanied by a secondary stellar-mass companion orbiting the host star that is redder and fainter than TOI-5205 and would dilute the transit.

Assuming no unresolved companions, the transit depth (δ_0) for a planet with area A_p crossing a star with area A_1 and luminosity $L_1(\lambda)$ is given by

$$\delta_0 = \left(\frac{A_p L_1(\lambda)}{A_1}\right)\frac{1}{L_1(\lambda)} = \frac{A_p}{A_1}. \tag{A3}$$

Instead, if there was an unresolved companion of later spectral type with luminosity $L_2(\lambda)$, where $L_2 < L_1$:

$$\delta(\lambda) = \left(\frac{A_p L_1(\lambda)}{A_1}\right)\frac{1}{L_1(\lambda) + L_2(\lambda)} \tag{A4}$$

$$\delta(\lambda) = \delta_0\left(\frac{L_1(\lambda)}{L_1(\lambda) + L_2(\lambda)}\right) \tag{A5}$$

$$\delta(\lambda) \propto \frac{1}{1 + L_2(\lambda)/L_1(\lambda)}. \tag{A6}$$

For $\lambda_2 > \lambda_1$,

$$\frac{L_2}{L_1}(\lambda_2) > \frac{L_2}{L_1}(\lambda_1) \tag{A7}$$

$$\text{i.e.,}\ \delta(\lambda_2) < \delta(\lambda_1). \tag{A8}$$

We obtained precise multifilter transit photometry from the 3.5 m ARC telescope (Figure 3) in the SDSS i' and g' filters. If there was a later spectral type unresolved companion (object 2) that was contaminating the photometry of the host star (object 1), it would result in different transit depths across different photometric bands. If we assume that we can compare the two transit depths (in g' and i') with a precision of ϵ, where ϵ is a small number, then

$$\frac{\delta(g')}{\delta(i')} = 1 + \epsilon. \tag{A9}$$

Then by this method, we can rule out all objects with luminosity less than $L_2(\lambda)$,

$$\frac{L_2}{L_1}(i') \Big/ \frac{L_2}{L_1}(g') = 1 + \epsilon. \tag{A10}$$

Using a separate dilution term for the ARCTIC transit in g', we probe for chromaticity in the transit depth between g' and i', but find the depths to be consistent to ∼10%, i.e., $\epsilon \sim 0.1$. We then use the SDSS transmission curves for the two filters, and compare the flux within the bandpass using BT-Settl CIFIST theoretical stellar spectra for a range of stellar masses (Allard et al. 2011, 2012). We conclude that this method would be sensitive to transit depth variations for an unresolved companion cooler than ∼3100 K or roughly 0.25 $M_\odot$ (Figure 10).

If there was a secondary stellar-mass object present in the system, i.e., a hierarchical system, it would be a source of dilution that would suggest a radius larger than the $\sim 1\,R_J$ estimated here. Due to the electron degeneracy pressure, objects around this size can range from Jovian planets to very-low-mass stars (M7–M8; Zapolsky & Salpeter 1969; Burrows et al. 2001). Therefore, if TOI-5205b had a larger radius (due to unaccounted dilution), it would have to be a late-type M dwarf or larger, which would make it at least 100× more massive than the $\sim 1\,M_J$ we measure (Table 4).

Finally, we put additional constraints on the possibility of a bound stellar companion, as follows:

1. Constraints from HPF spectra: We follow the procedure outlined in Kanodia et al. (2020) to place limits on any spatially unresolved stellar companion to TOI-5205 using the HPF spectra to quantify the lack of flux from a secondary object. We combine the spectra from a single epoch to obtain a higher S/N template for comparison, and then model the test spectra (TOI-3757) as a linear combination of a primary M dwarf (GJ 273) and a secondary companions (GJ 9066, GJ 1072, GJ 1111, and LSPM J0510+2714). The flux ratio between the secondary and primary star, F, is calculated as:

$$S_{\rm obs} = A((1-x)S_{\rm primary} + (x)S_{\rm secondary}) \quad \text{(A11)}$$

$$F = \frac{x}{1-x} \quad \text{(A12)}$$

where $S_{\rm obs}$ is the observed spectrum, $S_{\rm primary}$ is the primary spectrum, $S_{\rm secondary}$ represents the secondary spectrum, and A is the normalization constant. For a given primary and secondary template, we (i) perform a χ^2 minimization to shift the secondary spectrum in velocity space, (ii) add this shifted secondary spectrum to the primary, and (iii) fit for the value of x (and A) that best fits the observed spectrum. We perform this for a range of spectral types for the secondary from M4.5–M7 spanning velocity offsets of ± 150 km s^{-1}. We place a conservative upper limit for a secondary companion of flux ratio < 0.2 or $\Delta{\rm mag} \simeq 1.8$ for $|\Delta v| > 5$ km s^{-1}, using HPF order index 5 spanning 8650–8770 Å. The lower limit coincides with HPF's spectral resolution ($R \sim 55{,}000 \approx 5.5$ km s^{-1}). At lower velocity offsets, the degeneracy between the primary and secondary spectra prevents any meaningful flux ratio constraints.
2. Constraints from Gaia astrometry: Gaia DR3 (Vallenari et al. 2022) provides an additional astrometric constraint on the presence of unresolved bound companions using the re-normalized unit weight error (RUWE) metric. RUWE is sensitive to the change in the position of the primary target due to reflex motion caused by unresolved bound companions. For the single-star astrometric solution in use for Gaia DR3, this astrometric motion of the primary star around the center of mass would manifest as noise (Kervella et al. 2019), especially for orbital periods much shorter than the observing baseline for Gaia DR3 (~34 months). The commonly accepted threshold in the literature for this is RUWE $\gtrsim 1.4$, which correlates with the presence of a bound stellar companion in recent studies of stellar binaries (Belokurov et al. 2020; Penoyre et al. 2020; Gandhi et al. 2021). For TOI-5205, Gaia DR3 reports an RUWE of ~1.03, which is in agreement with a single-star astrometric solution.
3. Constraints from RVs: A joint fit of the photometry and RVs is used to estimate the planetary and system properties (Section 4). We also include a linear RV trend in the orbital solution while fitting the RVs. We estimate this to be consistent with 0, with the estimated RV trend $\sim 0.05^{+4.92}_{-5.08}$ m s^{-1} yr^{-1}. Assuming a circular orbit for a unresolved companion star, the maximum is at phase 0 (conjunction) and 180°, where the amplitude would be $2\pi K/P$, where K is the RV semi-amplitude on the primary star due to a hypothetical secondary, and P is its orbital period. However, given our short observing period (~30 days), we use this to only constrain companions with a maximum orbital period of ~60 days, or a semimajor axis of 0.2 au.

A.5. Galactic Kinematics

Using the systemic velocity from HPF and proper motion from Gaia DR3, we calculate the *UVW* velocities in the barycentric frame using `GALPY` (Bovy 2015).[36] We provide these velocities in Table 3, including those in the local standard of rest using the offsets from Schönrich et al. (2010). Using the BANYAN tool (Gagné et al. 2018), we classify TOI-5205 as a field star in the thin disk with very high probability (>99%; Bensby et al. 2014).

ORCID iDs

Shubham Kanodia https://orcid.org/0000-0001-8401-4300
Suvrath Mahadevan https://orcid.org/0000-0001-9596-7983
Jessica Libby-Roberts https://orcid.org/0000-0002-2990-7613
Gudmundur Stefansson https://orcid.org/0000-0001-7409-5688
Caleb I. Cañas https://orcid.org/0000-0003-4835-0619
Anjali A. A. Piette https://orcid.org/0000-0002-4487-5533
Alan Boss https://orcid.org/0000-0001-7119-1105
John Chambers https://orcid.org/0000-0001-9046-2265
Greg Zeimann https://orcid.org/0000-0003-2307-0629
Andrew Monson https://orcid.org/0000-0002-0048-2586
Paul Robertson https://orcid.org/0000-0003-0149-9678
Joe P. Ninan https://orcid.org/0000-0001-8720-5612
Andrea S. J. Lin https://orcid.org/0000-0002-9082-6337
Chad F. Bender https://orcid.org/0000-0003-4384-7220
William D. Cochran https://orcid.org/0000-0001-9662-3496
Scott A. Diddams https://orcid.org/0000-0002-2144-0764
Arvind F. Gupta https://orcid.org/0000-0002-5463-9980
Samuel Halverson https://orcid.org/0000-0003-1312-9391
Suzanne Hawley https://orcid.org/0000-0002-6629-4182
Henry A. Kobulnicky https://orcid.org/0000-0002-4475-4176
Andrew J. Metcalf https://orcid.org/0000-0001-5000-1018
Brock A. Parker https://orcid.org/0000-0001-9307-8170
Luke Powers https://orcid.org/0000-0002-5300-5353
Lawrence W. Ramsey https://orcid.org/0000-0002-4289-7958
Arpita Roy https://orcid.org/0000-0001-8127-5775
Christian Schwab https://orcid.org/0000-0002-0091-7105
Tera N. Swaby https://orcid.org/0000-0002-5817-202X
Ryan C. Terrien https://orcid.org/0000-0002-4788-8858
John Wisniewski https://orcid.org/0000-0001-9209-1808

References

Agol, E., Luger, R., & Foreman-Mackey, D. 2020, AJ, 159, 123
Allard, F., Homeier, D., & Freytag, B. 2011, ASPC, 448, 91
Allard, F., Homeier, D., & Freytag, B. 2012, RSPTA, 370, 2765
Anders, F., Khalatyan, A., Queiroz, A. B. A., et al. 2022, A&A, 658, A91
Anderson, D. E., Cleeves, L. I., Blake, G. A., et al. 2022, ApJ, 927, 229
Andrews, S. M., Rosenfeld, K. A., Kraus, A. L., & Wilner, D. J. 2013, ApJ, 771, 129
Andrews, S. M., & Williams, J. P. 2005, ApJ, 631, 1134

[36] With U toward the Galactic center, V toward the direction of Galactic spin, and W toward the North Galactic Pole (Johnson & Soderblom 1987).

Anglada-Escudé, G., & Butler, R. P. 2012, ApJS, 200, 15
Ansdell, M., Williams, J. P., Manara, C. F., et al. 2017, AJ, 153, 240
Ansdell, M., Williams, J. P., van der Marel, N., et al. 2016, ApJ, 828, 46
Astropy Collaboration, Price-Whelan, A. M., Sipocz, B. M., et al. 2018, AJ, 156, 123
Astudillo-Defru, N., Forveille, T., Bonfils, X., et al. 2017, A&A, 602, A88
Baraffe, I., & Chabrier, G. 2018, A&A, 619, A177
Baraffe, I., Chabrier, G., Allard, F., & Hauschildt, P. H. 1998, A&A, 337, 403
Barber, R. J., Strange, J. K., Hill, C., et al. 2014, MNRAS, 437, 1828
Barenfeld, S. A., Carpenter, J. M., Ricci, L., & Isella, A. 2016, ApJ, 827, 142
Batalha, N. E., Mandell, A., Pontoppidan, K., et al. 2017, PASP, 129, 064501
Bayliss, D., Gillen, E., Eigmüller, P., et al. 2018, MNRAS, 475, 4467
Beaugé, C., & Nesvorný, D. 2012, ApJ, 751, 119
Belokurov, V., Penoyre, Z., Oh, S., et al. 2020, MNRAS, 496, 1922
Benedict, G. F., Henry, T. J., Franz, O. G., et al. 2016, AJ, 152, 141
Bensby, T., Feltzing, S., & Oey, M. S. 2014, A&A, 562, A71
Bohlin, R. C., Savage, B. D., & Drake, J. F. 1978, ApJ, 224, 132
Bonfils, X., Delfosse, X., Udry, S., et al. 2005, A&A, 635, 635
Boss, A. P. 2006, ApJ, 643, 501
Boss, A. P. 2011, ApJ, 731, 74
Bovy, J. 2015, ApJS, 216, 29
Broyden, C. G. 1970, JApMa, 6, 76
Burn, R., Schlecker, M., Mordasini, C., et al. 2021, A&A, 656, A72
Burrows, A., Hubbard, W. B., Lunine, J. I., & Liebert, J. 2001, RvMP, 73, 719
Burt, J. A., Nielsen, L. D., Quinn, S. N., et al. 2020, AJ, 160, 153
Cañas, C. I., Kanodia, S., Bender, C. F., et al. 2022, AJ, 164, 50
Cañas, C. I., Stefansson, G., Kanodia, S., et al. 2020, AJ, 160, 147
Carpenter, J. M., Mamajek, E. E., Hillenbrand, L. A., & Meyer, M. R. 2006, ApJL, 651, L49
Cifuentes, C., Caballero, J. A., Cortés-Contreras, M., et al. 2020, A&A, 642, A115
Clough, S. A., Shephard, M. W., Mlawer, E. J., et al. 2005, JQSRT, 91, 233
Coleman, G. A. L., & Haworth, T. J. 2020, MNRAS, 496, L111
Collins, K. A., Kielkopf, J. F., Stassun, K. G., & Hessman, F. V. 2017, AJ, 153, 77
Covey, K. R., Ivezic, Ž., Schlegel, D., et al. 2007, AJ, 134, 2398
Creevey, O. L., Sordo, R., Pailler, F., et al. 2022, arXiv:2206.05864
Dash, S., Majumdar, L., Willacy, K., et al. 2022, ApJ, 932, 20
Dawson, R. I., & Johnson, J. A. 2012, ApJ, 756, 122
Dawson, R. I., & Johnson, J. A. 2018, ARA&A, 56, 175
Delfosse, X., Forveille, T., Ségransan, D., et al. 2000, A&A, 364, 217
Eisner, J. A., Arce, H. G., Ballering, N. P., et al. 2018, ApJ, 860, 77
Evans, C. J., Simard, L., Takami, H., et al. 2016a, Proc. SPIE, 9908, 99084C
Evans, K. C., Magnier, E. A., Metcalfe, N., et al. 2016b, The Pan-STARRS1 Surveys, Technical Report
Feiden, G. A., Skidmore, K., & Jao, W.-C. 2021, ApJ, 907, 53
Feinstein, A. D., Montet, B. T., Foreman-Mackey, D., et al. 2019, PASP, 131, 094502
Feng, F., Shectman, S. A., Clement, M. S., et al. 2020, ApJS, 250, 29
Fischer, D. A., & Valenti, J. 2005, ApJ, 622, 1102
Fletcher, R. 1970, CompJ, 13, 317
Ford, E. B. 2006, ApJ, 642, 505
Foreman-Mackey, D. 2018, RNAAS, 2, 31
Foreman-Mackey, D., Agol, E., Ambikasaran, S., & Angus, R. 2017, AJ, 154, 220
Foreman-Mackey, D., Luger, R., Agol, E., et al. 2021a, JOSS, 6, 3285
Foreman-Mackey, D., Savel, A., Luger, R., et al. 2021b, exoplanet-dev/exoplanet v0.4.4, Zenodo, doi:10.5281/zenodo.1998447
Gagné, J., Mamajek, E. E., Malo, L., et al. 2018, ApJ, 856, 23
Gaidos, E., Mann, A. W., Rojas-Ayala, B., et al. 2022, MNRAS, 514, 1386
Gan, T., Lin, Z., Wang, S. X., et al. 2022, MNRAS, 511, 83
Gandhi, P., Buckley, D. A. H., Charles, P. A., et al. 2021, MNRAS, 510, 3885
Gandhi, S., & Madhusudhan, N. 2017, MNRAS, 472, 2334
Gandhi, S., & Madhusudhan, N. 2019, MNRAS, 485, 5817
Ghezzi, L., Cunha, K., Smith, V. V., et al. 2010, ApJ, 720, 1290
Ghezzi, L., Montet, B. T., & Johnson, J. A. 2018, ApJ, 860, 109
Ginsburg, A., Sipocz, B. M., Brasseur, C. E., et al. 2019, AJ, 157, 98
Goldfarb, D. 1970, MaCom, 24, 23
Gonzalez, G. 1997, MNRAS, 285, 403
Greaves, J. S., & Rice, W. K. M. 2010, MNRAS, 407, 1981
Gullikson, K., Dodson-Robinson, S., & Kraus, A. 2014, AJ, 148, 53
Harrington, R. G. 1952, PASP, 64, 275
Harris, G. J., Tennyson, J., Kaminsky, B. M., Pavlenko, Y. V., & Jones, H. R. A. 2006, MNRAS, 367, 400
Harris, C. R., Millman, K. J., & van der Walt, S. J. 2020, Natur, 585, 357
Hartman, J. D., Bayliss, D., Brahm, R., et al. 2015, AJ, 149, 166
Helled, R., & Bodenheimer, P. 2010, Icar, 207, 503
Helled, R., Bodenheimer, P., Podolak, M., et al. 2014, in Protostars and Planets VI, ed. H. Beuther et al. (Tucson, AZ: Univ. Arizona Press), 643
Helled, R., & Lunine, A. 2021, Planet Formation, Tech. Rep.
Helled, R., & Lunine, J. 2014, MNRAS, 441, 2273
Heng, K., & Tsai, S.-M. 2016, ApJ, 829, 104
Henry, T., Jao, W.-C., Subasavage, J., et al. 2006, AJ, 132, 2360
Henry, T. J., & McCarthy, D. W., Jr. 1993, AJ, 106, 773
Hobbs, R., Shorttle, O., & Madhusudhan, N. 2022, MNRAS, 516, 1032
Hoffman, M. D., & Gelman, A. 2014, JMLR, 15, 1593
Howell, S. B., Everett, M. E., Sherry, W., Horch, E., & Ciardi, D. R. 2011, AJ, 142, 19
Huang, C. X., Vanderburg, A., Pál, A., et al. 2020, RNAAS, 4, 204
Huehnerhoff, J., Ketzeback, W., Bradley, A., et al. 2016, Proc. SPIE, 9908, 99085H
Hunter, J. D. 2007, CSE, 9, 90
Ida, S., & Lin, D. N. C. 2005, ApJ, 626, 1045
Jao, W.-C., & Feiden, G. A. 2020, AJ, 160, 102
Jao, W.-C., Henry, T. J., Gies, D. R., & Hambly, N. C. 2018, ApJL, 861, L11
Jenkins, J. M., Caldwell, D. A., Chandrasekaran, H., et al. 2010, ApJL, 713, L87
Johnson, D. R. H., & Soderblom, D. R. 1987, AJ, 93, 864
Johnson, J. A., Gazak, J. Z., Apps, K., et al. 2012, AJ, 143, 111
Johnson, J. A., Howard, A. W., Marcy, G. W., et al. 2010, PASP, 122, 149
Jordán, A., Hartman, J. D., Bayliss, D., et al. 2022, AJ, 163, 125
Kanodia, S., Cañas, C. I., Stefansson, G., et al. 2020, ApJ, 899, 29
Kanodia, S., Libby-Roberts, J., Cañas, C. I., et al. 2022, AJ, 164, 81
Kanodia, S., Mahadevan, S., Ramsey, L. W., et al. 2018, SPIE Proc., 0702, 107026Q
Kanodia, S., & Wright, J. 2018, RNAAS, 2, 4
Kasper, D. H., Ellis, T. G., Yeigh, R. R., et al. 2016, PASP, 128, 105005
Kempton, E.-M.-R., Bean, J. L., Louie, D. R., et al. 2018, PASP, 130, 114401
Kempton, E.-M.-R., Lupu, R., Owusu-Asare, A., Slough, P., & Cale, B. 2017, PASP, 129, 044402
Kervella, P., Arenou, F., Mignard, F., & Thévenin, F. 2019, A&A, 623, A72
Kiman, R., Schmidt, S. J., Angus, R., et al. 2019, AJ, 157, 231
Kipping, D. M. 2013, MNRAS, 435, 2152
Kirkpatrick, J. D., Henry, T. J., & McCarthy, D. W., Jr. 1991, ApJS, 77, 417
Kley, W., & Nelson, R. P. 2012, ARA&A, 50, 211
Knierim, H., Shibata, S., & Helled, R. 2022, A&A, 665, L5
Kochanek, C. S., Shappee, B. J., Stanek, K. Z., et al. 2017, PASP, 129, 104502
Kroupa, P., & Tout, C. A. 1997, MNRAS, 287, 402
Kroupa, P., Tout, C. A., & Gilmore, G. 1990, MNRAS, 244, 76
Kumar, R., Carroll, C., Hartikainen, A., & Martin, O. A. 2019, JOSS, 4, 1143
Kunimoto, M., Daylan, T., Guerrero, N., et al. 2022, ApJS, 259, 33
Laughlin, G., Bodenheimer, P., & Adams, F. C. 2004, ApJL, 612, L73
Lee, H., Chonis, T. S., Hill, G. J., et al. 2010, Proc. SPIE, 7735, 77357H
Lee, J., Song, I., & Murphy, S. 2020, MNRAS, 494, 62
Lightkurve Collaboration, Cardoso, J. V. D., Hedges, C., et al. 2018, Lightkurve: Kepler and TESS time series analysis in Python, Astrophysics Source Code Library, ascl:1812.013
Limber, D. N. 1958, ApJ, 127, 363
Limber, D. N. 1960, ASPL, 8, 127
Lin, J. W., Lee, E. J., & Chiang, E. 2018, MNRAS, 480, 4338
Lomb, N. R. 1976, Ap&SS, 39, 447
Luger, R., Agol, E., Foreman-Mackey, D., et al. 2019, AJ, 157, 64
MacDonald, J., & Gizis, J. 2018, MNRAS, 480, 1711
Madhusudhan, N., Amin, M. A., & Kennedy, G. M. 2014, ApJL, 794, L12
Mahadevan, S., McLean, I. S., Ramsay, S. K., et al. 2012, Proc. SPIE, 8446, 84461S
Maldonado, J., Micela, G., Baratella, M., et al. 2020, A&A, 644, A68
Maldonado, J., Villaver, E., Eiroa, C., & Micela, G. 2019, A&A, 624, A94
Mandel, K., & Agol, E. 2002, ApJL, 580, L171
Mann, A. W., Dupuy, T., Kraus, A. L., et al. 2019, ApJ, 871, 63
Mann, A. W., Feiden, G. A., Gaidos, E., Boyajian, T., & von Braun, K. 2015, ApJ, 804, 64
Mann, A. W., Feiden, G. A., Gaidos, E., Boyajian, T., & von Braun, K. 2016, ApJ, 819, 87
Mann, A. W., Wood, M. L., Schmidt, S. P., et al. 2022, AJ, 163, 156
Masci, F. J., Laher, R. R., Rusholme, B., et al. 2019, PASP, 131, 018003
McKinney, W. 2010, in Proc. 9th Python in Science Conf., ed. S. v. d. Walt & J. Millman (Austin, TX: SciPy), 56
Metcalf, A. J., Anderson, T., Bender, C. F., et al. 2019, Optic, 6, 233
Minkowski, R. L., & Abell, G. O. 1963, Basic Astronomical Data: Stars and Stellar Systems (Chicago, IL: Univ. Chicago Press), 481
Miotello, A., van Dishoeck, E. F., Williams, J. P., et al. 2017, A&A, 599, A113

Monson, A. J., Beaton, R. L., Scowcroft, V., et al. 2017, AJ, 153, 96
Morales, J. C., Mustill, A. J., Ribas, I., et al. 2019, Sci, 365, 1441
Mulders, G. D., Pascucci, I., & Apai, D. 2015, ApJ, 798, 112
Najita, J. R., & Kenyon, S. J. 2014, MNRAS, 445, 3315
NASA Exoplanet Archive 2022, Planetary Systems Composite Parameters, Version: 2022-08-20 00:00, NExScI-Caltech/IPAC, doi:10.26133/NEA13
Neves, V., Bonfils, X., Santos, N. C., et al. 2012, A&A, 538, A25
Ninan, J. P., Bender, C. F., Mahadevan, S., et al. 2018, Proc. SPIE, 0709, 107092U
Öberg, K. I., Murray-Clay, R., & Bergin, E. A. 2011, ApJL, 743, L16
Oliphant, T. 2006, NumPy: A Guide to NumPy, http://www.numpy.org/
Oliphant, T. E. 2007, CSE, 9, 10
Parviainen, H., Palle, E., Zapatero-Osorio, M. R., et al. 2021, A&A, 645, A16
Pascucci, I., Testi, L., Herczeg, G. J., et al. 2016, ApJ, 831, 125
Passegger, V. M., Bello-García, A., Ordieres-Meré, J., et al. 2022, A&A, 658, A194
Pecaut, M. J., & Mamajek, E. E. 2016, MNRAS, 461, 794
Penoyre, Z., Belokurov, V., Wyn Evans, N., Everall, A., & Koposov, S. E. 2020, MNRAS, 495, 321
Pérez, F., & Granger, B. E. 2007, CSE, 9, 21
Persson, S. E., Murphy, D. C., Smee, S., et al. 2013, PASP, 125, 654
Piette, A. A. A., & Madhusudhan, N. 2020, ApJ, 904, 154
Piette, A. A. A., Madhusudhan, N., McKemmish, L. K., et al. 2020, MNRAS, 496, 3870
Pollack, J. B., Hubickyj, O., Bodenheimer, P., et al. 1996, Icar, 124, 62
Quirrenbach, A., Passegger, V. M., Trifonov, T., et al. 2022, A&A, 663, A48
Rabus, M., Lachaume, R., Jordán, A., et al. 2019, MNRAS, 484, 2674
Ramsay, S. K., McLean, I. S., Takami, H., et al. 2014, Proc. SPIE, 9147, 91471G
Ramsey, L. W., Adams, M. T., Barnes, T. G., III, et al. 1998, Proc. SPIE, 3352, 34
Reiners, A., & Basri, G. 2008, ApJ, 684, 1390
Reylé, C., Jardine, K., Fouqué, P., et al. 2021, A&A, 650, A201
Ribas, A., Merin, B., Bouy, H., & Maud, L. T. 2014, A&A, 561, A54
Richard, C., Gordon, I. E., Rothman, L. S., et al. 2012, JQSRT, 113, 1276
Ricker, G. R., Winn, J. N., Vanderspek, R., et al. 2014, JATIS, 1, 014003
Robitaille, T. P., Tollerud, E. J., Greenfield, P., et al. 2013, A&A, 558, A33
Rosotti, G. P., Clarke, C. J., Manara, C. F., & Facchini, S. 2017, MNRAS, 468, 1631
Rothman, L. S., Gordon, I. E., Babikov, Y., et al. 2013, JQSRT, 130, 4
Rothman, L. S., Gordon, I. E., Barber, R. J., et al. 2010, JQSRT, 111, 2139
Roulston, B. R., Green, P. J., & Kesseli, A. Y. 2020, ApJS, 249, 34
Salvatier, J., Wiecki, T. V., & Fonnesbeck, C. 2016, PeerJ Computer Science, 2, e55
Santos, N. C., Adibekyan, V., Figueira, P., et al. 2017, A&A, 603, A30
Santos, N. C., Israelian, G., & Mayor, M. 2001, A&A, 373, 1019
Scargle, J. D. 1982, ApJ, 263, 835
Schlaufman, K. C. 2018, ApJ, 853, 37
Schlaufman, K. C., & Laughlin, G. 2010, A&A, 519, A105
Schlecker, M., Burn, R., Sabotta, S., et al. 2022, A&A, 664, A180
Schönrich, R., Binney, J., & Dehnen, W. 2010, MNRAS, 403, 1829
Schweitzer, A., Passegger, V. M., Cifuentes, C., et al. 2019, A&A, 625, A68
Scott, N. J., Howell, S. B., Horch, E. P., & Everett, M. E. 2018, PASP, 130, 054502
Shanno, D. F. 1970, MaCom, 24, 647
Shetrone, M., Cornell, M., Fowler, J., et al. 2007, PASP, 119, 556
Silverberg, S. M., Wisniewski, J. P., Kuchner, M. J., et al. 2020, ApJ, 890, 106
Silverstein, M. L., Schlieder, J. E., Barclay, T., et al. 2022, AJ, 163, 151
Sousa, S. G., Santos, N. C., Israelian, G., Mayor, M., & Udry, S. 2011, A&A, 533, A141
Stassun, K. G., Oelkers, R. J., Paegert, M., et al. 2019, AJ, 158, 138
Stassun, K. G., Oelkers, R. J., Pepper, J., et al. 2018, AJ, 156, 102
Stefansson, G., Cañas, C., Wisniewski, J., et al. 2020, AJ, 159, 100
Stefansson, G., Hearty, F., Robertson, P., et al. 2016, ApJ, 833, 175
Stefansson, G., Mahadevan, S., Hebb, L., et al. 2017, ApJ, 848, 9
Stetson, P. B. 1987, PASP, 99, 191
Stetson, P. B., & Harris, W. E. 1988, AJ, 96, 909
The Theano Development Team, Al-Rfou, R., Alain, G., et al. 2016, arXiv:1605.02688
Thorngren, D. P., Fortney, J. J., Murray-Clay, R. A., & Lopez, E. D. 2016, ApJ, 831, 64
Tonry, J. L., Denneau, L., Heinze, A. N., et al. 2018, PASP, 130, 064505
Trifonov, T., Kürster, M., Zechmeister, M., et al. 2018, A&A, 609, A117
Vallenari, A., Arenou, F., Bellazzini, M., et al. 2022, Gaia DR3 Documentation (Paris: ESA), 19
van Saders, J. L., & Pinsonneault, M. H. 2012, ApJ, 751, 98
VanderPlas, J. T. 2018, ApJS, 236, 16
Virtanen, P., Gommers, R., Oliphant, T. E., et al. 2020, NatMe, 17, 261
Vorobyov, E. I. 2011, ApJ, 729, 146
West, A. A., Weisenburger, K. L., Irwin, J., et al. 2015, ApJ, 812, 3
Williams, J. P., & Best, W. M. J. 2014, ApJ, 788, 59
Wittenmyer, R. A., Tuomi, M., Butler, R. P., et al. 2014, ApJ, 791, 114
Wright, J. T., & Eastman, J. D. 2014, PASP, 126, 838
Yan, R., Chen, Y., Lazarz, D., et al. 2019, ApJ, 883, 175
Yee, S. W., Petigura, E. A., & von Braun, K. v. 2017, ApJ, 836, 77
Yurchenko, S. N., Barber, R. J., & Tennyson, J. 2011, MNRAS, 413, 1828
Yurchenko, S. N., & Tennyson, J. 2014, MNRAS, 440, 1649
Yurchenko, S. N., Tennyson, J., Barber, R. J., & Thiel, W. 2013, JMoSp, 291, 69
Zapolsky, H. S., & Salpeter, E. E. 1969, ApJ, 158, 809
Zechmeister, M., & Kürster, M. 2009, A&A, 496, 577
Zechmeister, M., Reiners, A., Amado, P. J., et al. 2018, A&A, 609, A12